CrossMark

Two-Dimensional Magnetotelluric Modelling of Ore Deposits: Improvements in Model Constraints by Inclusion of Borehole Measurements

Thomas Kalscheuer[1] [iD] · Niklas Juhojuntti[2] · Katri Vaittinen[3]

Abstract A combination of magnetotelluric (MT) measurements on the surface and in boreholes (without metal casing) can be expected to enhance resolution and reduce the ambiguity in models of electrical resistivity derived from MT surface measurements alone. In order to quantify potential improvement in inversion models and to aid design of electromagnetic (EM) borehole sensors, we considered two synthetic 2D models containing ore bodies down to 3000 m depth (the first with two dipping conductors in resistive crystalline host rock and the second with three mineralisation zones in a sedimentary succession exhibiting only moderate resistivity contrasts). We computed 2D inversion models from the forward responses based on combinations of surface impedance measurements and borehole measurements such as (1) skin-effect transfer functions relating horizontal magnetic fields at depth to those on the surface, (2) vertical magnetic transfer functions relating vertical magnetic fields at depth to horizontal magnetic fields on the surface and (3) vertical electric transfer functions relating vertical electric fields at depth to horizontal magnetic fields on the surface. Whereas skin-effect transfer functions are sensitive to the resistivity of the background medium and 2D anomalies, the vertical magnetic and electric field transfer functions have the disadvantage that they are comparatively insensitive to the resistivity of the layered background medium. This insensitivity introduces convergence problems in the inversion of data from structures with strong 2D resistivity contrasts. Hence, we adjusted the inversion approach to a three-step procedure, where (1) an initial inversion model is computed from surface impedance measurements,

✉ Thomas Kalscheuer
  thomas.kalscheuer@geo.uu.se

  Niklas Juhojuntti
  niklas.juhojuntti@lkab.com

  Katri Vaittinen
  katri.vaittinen@boliden.com

[1] Department of Earth Sciences, Uppsala University, Villavägen 16, 752 36 Uppsala, Sweden

[2] Luossavaara-Kiirunavaara AB (LKAB), Kiirunavaaravägen 1, 981 86 Kiruna, Sweden

[3] Boliden Finnex Oy, Polvijärvi Exploration Office, Polvijärventie 22, 83700 Polvijärvi, Finland

(2) this inversion model from surface impedances is used as the initial model for a joint inversion of surface impedances and skin-effect transfer functions and (3) the joint inversion model derived from the surface impedances and skin-effect transfer functions is used as the initial model for the inversion of the surface impedances, skin-effect transfer functions and vertical magnetic and electric transfer functions. For both synthetic examples, the inversion models resulting from surface and borehole measurements have higher similarity to the true models than models computed exclusively from surface measurements. However, the most prominent improvements were obtained for the first example, in which a deep small-sized ore body is more easily distinguished from a shallow main ore body penetrated by a borehole and the extent of the shadow zone (a conductive artefact) underneath the main conductor is strongly reduced. Formal model error and resolution analysis demonstrated that predominantly the skin-effect transfer functions improve model resolution at depth below the sensors and at distance of $\sim$ 300–1000 m laterally off a borehole, whereas the vertical electric and magnetic transfer functions improve resolution along the borehole and in its immediate vicinity. Furthermore, we studied the signal levels at depth and provided specifications of borehole magnetic and electric field sensors to be developed in a future project. Our results suggest that three-component SQUID and fluxgate magnetometers should be developed to facilitate borehole MT measurements at signal frequencies above and below 1 Hz, respectively.

1 Introduction

1.1 MT Methods in Exploring Deep Ore Deposits

In magnetotelluric methods (Vozoff 1991; Berdichevsky and Dmitriev 2008; Chave and Jones 2012), naturally occurring electric and magnetic fields are used to sense the electrical conductivity structure of the Earth. In combination, audiomagnetotelluric (AMT) data (frequencies $f = 1$–10,000 Hz), with signals originating from the global lightning distribution, and broadband magnetotelluric (BBMT) data (frequencies $f = 0.001$–300 Hz), comprising AMT signals and lower-frequency ($f < 1$ Hz) signals caused by magnetospheric and ionospheric currents, explore a depth range of a few tens of metres down to a few tens of kilometres or more. This makes MT methods particularly suitable to investigate deep-seated (500–4000 m) mineral deposits. Where AMT signal levels are low, e.g., in the dead band at $\sim$ 800–3000 Hz (Garcia and Jones 2002), the controlled-source audiomagnetotelluric method (CSAMT, $f = 1$–10000 Hz, Zonge and Hughes 1991) is routinely applied. Consequently, MT methods have a long-standing history in the investigation of mineral deposits (Strangway et al. 1973; Meju 2002; Jones 2017) with field cases reported from, for instance, copper, gold, lead, silver and zinc deposits (Kellett et al. 1993; Garcia Juanatey et al. 2013a, b; Hübert et al. 2013; Hu et al. 2013), copper, gold and iron deposits (Heinson et al. 2006), copper and iron deposits (Chouteau et al. 1997; Jones and Garcia 2003), copper, iron and zinc deposits (Basokur et al. 1997), copper, lead and zinc deposits (Sasaki et al. 1992; Bastani et al. 2009), copper and nickel deposits (Lakanen 1986; Livelybrooks et al. 1996; Jones et al. 1997; Balch et al. 1998; Stevens and McNeice 1998; Zhang et al. 1998; Watts and Balch 2000; King 2007; Xiao et al. 2011; Varentsov et al. 2013; Le et al. 2016a), copper, silver and zinc deposits (Gordon 2007), gold deposits (Jones et al. 1997; Liu et al. 2006; Howe et al. 2014; Takam Takougang et al. 2015; Hübert et al. 2016; Le et al. 2016b), and uranium deposits (Leppin and Goldak 2005; Tuncer et al. 2006; Farquharson and Craven 2009; Goldak et al. 2010; Hautot et al. 2011;

Crowe et al. 2013). However, in conductivity models computed from surface MT and CSAMT measurements, the upper edges of conductive mineralisation zones are imaged with far greater resolution than the lower edges, which appear smeared out towards greater depth, making the investigation of possible deeper mineralisation difficult (Bedrosian 2007). This is a well-known phenomenon of inductive EM methods that conductive targets screen the regions below them (e.g., Jones 1999; Kalscheuer et al. 2015). A possible but insufficiently explored remedy to constrain geological structure underneath conductive mineral deposits or conductive overburden in general is to record MT signals at depth underneath the overburden, e.g., in boreholes or galleries, as proposed by Queralt et al. (2007).

1.2 MT Measurements at Depth in Boreholes, Galleries and the Oceans

To our knowledge, vertical telluric fields, i.e. natural vertical electric fields at MT frequencies, were first measured in a borehole, shown to correlate with simultaneously measured changes in horizontal magnetic and electric fields on the surface and put into causative relation to lateral conductivity contrasts by Forbush (1933). Later studies by Jones and Geldart (1967a, b), Bahr (1983) and Bahr and Eisel (1990) corroborated Forbush's findings. Bahr (1983) and Bahr and Eisel (1990) presented transfer functions (tensorial impedances) between the horizontal electric fields measured on the surface and the vertical electric field measured at depth as output channels and the horizontal magnetic fields measured on the surface as input channels. Using these transfer functions, Bahr (1983) and Bahr and Eisel (1990) computed regional strike angles that do not exhibit the 90-degree ambiguity in impedances retrieved from horizontal fields only. Thus, Bahr's and Bahr and Eisel's approach is, in principle, similar to removing the ambiguity by considering a combination of impedances and vertical magnetic transfer functions in standard MT surface measurements. Considering distortion from shallow inhomogeneities, Bahr (1983) recorded vertical electric fields using electrodes at shallow depth and just 1 m vertical spacing, and related the impedances of these vertical electric fields to shallow local anomalies using 2D forward modelling.

The first attempts to record plane-wave electromagnetic (EM) fields in boreholes for the purpose of mineral prospecting were related to development of a borehole receiver system by the Mineral Exploration Research Institute in Montreal and the Geological Survey of Canada (Roy 1984; Hayles and Dyck 1987; Dyck 1991). This system recorded the axial magnetic and electric field components at very low frequency (VLF) of 3–30 kHz using the horizontal magnetic fields on the surface as reference. An extension to recording all three components of the magnetic field at depth was developed in the 1990s (Mwenifumbo et al. 1997). Since powerful remote VLF military transmitters are used as sources, three-component (3C) VLF fields can be recorded using small induction coils that fit into standard boreholes (cf. next section). Owing to the comparatively high signal frequencies, the depth of investigation range of this method is limited to roughly the upper 300 m. As far as we know, no efforts of quantitative interpretation or inversion of these VLF borehole data have been documented.

Considering synthetic models, West and Ward (1988), Sasaki et al. (1992) and Queralt et al. (2007) demonstrated that a combination of surface and borehole or in-mine AMT and CSAMT measurements (using sources at the Earth's surface) can help overcome the limited resolution below conductive overburden provided by surface measurements. While the lateral extent of mines may allow in-mine measurements of horizontal electric and magnetic fields (Queralt et al. 2007), borehole AMT and CSAMT measurements would be

limited to the measurement of the axial component of the magnetic or electric field along the borehole. In West and Ward's (1988) synthetic 3D AMT forward modelling studies and in Sasaki et al.'s (1992) synthetic 2D AMT inverse modelling studies, these axial components were normalised by horizontal magnetic fields simulated at the Earth's surface. In vertical boreholes, such data have no sensitivity to the resistivity distribution of planar layered models (Ward and Hohmann 1987). However, for 2D and 3D models, there is limited sensitivity to the normal (layered background) resistivity distribution, mostly in the form of sensitivity to the anomalous resistivity contrast (Bahr 1983; West and Ward 1988). At present, AMT measurements of the off-axial components of the magnetic field in boreholes are not possible due to difficulties in sensor design (cf. next section).

In contrast to AMT borehole measurements, which presently are limited to the axial field components, the vertical gradient magnetometry (VGM) or skin-effect transfer functions presented by Jones (1983), Spitzer (1993) and Schmucker et al. (2009) rely upon horizontal magnetic fields measured in boreholes at MT frequencies of less than 1 Hz using 3C fluxgate magnetometers (cf. next section). In the VGM transfer functions, horizontal magnetic fields at adjacent depth levels are considered. Skin-effect transfer functions relate the horizontal magnetic fields at depth to those recorded on the surface. Unfortunately, fluxgates do not offer sufficient sensitivity in the AMT frequency range. Furthermore, the skin-effect transfer function field data collected by Spitzer (1993) and Schmucker et al. (2009) in the MT frequency range have lower quality than their MT field data collected on the surface. Whereas Jones (1983) studied 1D and 2D forward simulations of VGM data, Spitzer (1993) and Schmucker et al. (2009) explained skin-effect transfer function field data using 2D forward modelling. VGM and skin-effect transfer function data have been demonstrated to be sensitive predominantly to structure at depth below the borehole sensor, including the normal resistivity distribution.

In Sasaki et al.'s (1992) synthetic 2D inverse modelling studies, the employed borehole transfer functions pertain to the transverse magnetic (TM) mode and are the vertical electrical and horizontal magnetic fields normalised by the horizontal magnetic field on the surface. The latter transfer function is one of the skin-effect transfer functions presented by Spitzer (1993) and Schmucker et al. (2009). Neither 2D single inversions of transverse electric (TE) mode borehole transfer functions nor 2D joint inversions of TM-mode and TE-mode borehole transfer functions have been previously presented. However, for 2D models, TE-mode responses are sensitive to conductive structures, whereas TM-mode responses are predominantly sensitive to conductivity contrasts (e.g., Berdichevsky et al. 1998; Pedersen and Engels 2005). This complementary nature of TE-mode and TM-mode responses has long been understood and exploited in the interpretation of MT surface measurements. It is generally desirable to jointly invert TE-mode and TM-mode surface and borehole measurements.

In marine geophysical campaigns, geomagnetic variation measurements connect horizontal magnetic fields on the ocean floor and horizontal magnetic fields measured at a nearby coastal station using transfer functions very similar to those of the VGM method (e.g., Law and Greenhouse 1981; Jegen and Edwards 1998; Joseph et al. 2000). This marine VGM method was used with success and was later augmented with measurements of marine MT impedance tensors as measurements of marine electric fields became possible (Constable 2013).

1.3 Other Borehole Electromagnetic Methods

For the last 40–50 years, controlled-source frequency-domain and time-domain borehole electromagnetic (BHEM) methods (Dyck 1991; Asten 1996; Spies 1996) have been two of the standard tools in mineral exploration. In typical BHEM surveys, transmitter loops with more than 200 m side length are deployed on the surface of the ground, and magnetic field data are collected in boreholes and on the surface (e.g., Boyd and Wiles 1984; Pantze et al. 1986; Dyck 1991; Bishop et al. 2000; Hattula and Rekola 2000; Spicer 2016). In order to illuminate deposits from different angles, and thus to determine dip angle, along-dip extent and along-strike extent, individual boreholes are surveyed using a combination of different transmitter loops (e.g., Asten 1996). Until the mid-1980s, axial induction coil sensors were commonly used. However, the added value of 3C measurements led to development of 3C magnetic field sensors (e.g., Pantze et al. 1986; Cull 1996a, b; Hughes and Ravenhurst 1996; Duncan et al. 1998; Elders and Asten 2004). Simultaneously, receiver systems were improved, and modern instruments have enhanced filtering and stacking capability for derivation of processed data in the field and the recording of raw time series for advanced processing in the laboratory (e.g., Duncan et al. 1998; Elders and Asten 2004).

Magnetometric resistivity (MMR) methods (Edwards and Nabighian 1991) employ galvanically coupled sources with low signal frequencies. Thus, these methods generate current systems very much similar to electrical resistance tomography (ERT) methods. However, rather than measuring differences in electric potential between two electrodes, as in the ERT method, the components of the magnetic flux vector are measured leading to insensitivity to layered structures for MMR measurements made on the Earth's surface. Owing to the usage of galvanically coupled sources and magnetic field receivers, MMR measurements are sensitive to conductivity contrasts but not to absolute conductivity (Bishop et al. 1997; Asten 2001; Chen et al. 2002; Godber and Bishop 2007). In comparison, BHEM measurements are predominantly sensitive to conductive structures. This suggests a complementary nature of MMR and BHEM methods in studying mineral deposits. The cross-hole magnetometric resistivity (source and receivers in distinct boreholes; Nabighian et al. 1984) and down-hole magnetometric resistivity (DHMMR; source on surface extended along strike and borehole receivers; Asten 1988) methods have been used with success in mineral exploration and led to discoveries of ore deposits that did not generate anomalous BHEM signals (e.g., Bishop et al. 1997, 2000). Field evidence (Asten 1988; Bishop et al. 1997) and numerical simulations (Chen et al. 2002) suggest that the sensitivity of DHMMR and surface MMR data, respectively, is limited to lateral distances $\lesssim 500$ m off the borehole or receiver site, whereas BHEM methods may be sensitive to a comparable or smaller region around the borehole. Further, spatial resolution reported for DHMMR is poorer than that of BHEM (Asten 1988; Bishop et al. 1997). To ascertain that the spatial resolution and the investigation range of a given method (or instrument) are suitable to resolve a given geological structure, careful forward modelling, based on all available information, and consideration of the local noise conditions are required.

In the above description of BHEM and MMR systems, we have focused on surface-to-borehole systems that use extended surface sources and borehole receivers. In the context of prospecting deep mineral deposits, consideration of extended sources is motivated by the higher penetration depth of the generated signals. For shallower or smaller targets, systems that operate small dipole sources and receivers at higher frequencies and in single-hole or cross-hole configurations are more suitable to achieve resolution at smaller scales.

Descriptions of these methods can be found in Dyck (1991), Spies (1996) and Fullagar et al. (2000).

In comparison with BHEM and MMR methods, MT methods have both advantages and disadvantages. Both AMT and BBMT surveys offer much larger penetration depth than BHEM and MMR methods, which makes them very attractive tools in the current quest for targets at more than 500 m depth. As described above, MT data are sensitive to both conductive and resistive structures. This is an advantage over the sensitivities to conductive structures and conductivity contrasts provided by the BHEM and MMR methods, respectively, when only one of the latter methods is used. Since natural sources are used, omission of a transmitter crew either leads to a significant reduction in staff or frees resources to deploy another receiver crew. In terms of man hours, these advantages are, to some extent, offset by the need for extended recording times to capture the weak natural-source signals. More importantly, omission of a transmitter removes the single most important safety issue of guarding humans and animals from electric shock. In particular close to infrastructure, MT signals can have very low signal-to-noise ratios. Further, infrastructure can lead to bias through contamination with systematic noise that cannot be removed with present filtering techniques. In the worst case, this problem can render MT measurements useless when carried out in the vicinity of operating mines. The only means of increasing the signal-to-noise ratio is to resort to controlled-source electromagnetic (CSEM) methods such as BHEM, MMR and CSAMT. When depth penetration comparable to AMT is demanded, the CSAMT method may be a suitable substitute. CSAMT data recorded in the far-field zone of the source (Zonge and Hughes 1991) can be interpreted with the 2D inversion for AMT and BBMT data presented here.

1.4 Borehole Sensors and Conditions

In ore exploration, the diameters of standard boreholes vary between 5.5 and 8 cm posing serious limitations on the design of sensors. Over the last two decades, there has been significant progress in the development of 3C magnetic field borehole sensors for MT methods and CSEM methods, such as the frequency-domain and time-domain BHEM methods. Existing 3C magnetic field sensors are divided into the following categories:

- *Fluxgate magnetometers* utilise the non-linearity of the hysteresis curve of a magnetically susceptible core to measure the magnetic flux vector **B**. Owing to their limited size of a few cm^3, fluxgates fit into slim boreholes. The first 3C borehole fluxgate magnetometer for the lower MT frequency range (0.0001–1 Hz) was developed by the University of Göttingen, Germany, during the 1980s (Steveling et al. 1991; Spitzer 1993; Schmucker et al. 2009). However, fluxgates do not offer sufficient sensitivity in the AMT frequency range of 1–10,000 Hz, where sensor noise is high at $\sim$ 1000–10000 fT/$\sqrt{\text{Hz}}$. Since the signal levels in CSEM measurements are typically higher than in AMT measurements, 3C borehole fluxgates are regularly used in BHEM measurements.
- *Induction coils* measure the temporal change $\partial \mathbf{B}/\partial t$ of the magnetic flux vector **B**. For AMT surface measurements at frequencies of 1–10,000 Hz, induction coils have comparatively low sensor noise ($\sim$ 10–100 fT/$\sqrt{\text{Hz}}$) and, thus, have set the standard for decades. However, we are not aware of any successful AMT borehole measurements using induction coils. Owing to space limitations in the borehole probe in the off-axial directions, induction coils cannot reach a sensitivity level acceptable for AMT measurements in the off-axial directions of boreholes. For the controlled-source

BHEM methods, 3C borehole induction magnetometers are used on a routine basis (e.g., Pantze et al. 1986; Cull 1996a, b; Duncan et al. 1998; Elders and Asten 2004). Even though signal levels generated by BHEM sources are typically higher than those of AMT, the two off-axial components of the BHEM magnetic field are still problematic with respect to noise.

- *Superconducting quantum interference devices* (SQUIDs) measure the magnetic flux vector **B** and may be applicable in several geophysical magnetic and electromagnetic methods using frequencies from 0 Hz to roughly 10,000 Hz (Clarke 1983). However, they need to be held at low temperature. High-temperature superconductor (HTS) and low-temperature superconductor (LTS) SQUIDs operate at 77 K ($-196\,°C$) using immersion in liquid nitrogen and 4.2 K ($-269\,°C$) using immersion in liquid helium, respectively (e.g., Le Roux and Macnae 2007). LTS SQUIDs have the advantage of higher sensitivity as compared to HTS SQUIDs (sensor noise $\sim 1\,fT/\sqrt{Hz}$ versus $> 10\,fT/\sqrt{Hz}$ at 10–10,000 Hz). In the 1980s, there was an initial period of higher usage of SQUIDs in MT field campaigns (e.g., Berktold 1983; Hermance et al. 1984). However, it was soon realised that the need for cryogenic cooling with liquid nitrogen or helium and the size of early SQUID sensors made them less practical for field campaigns than induction coil sensors (Chave and Booker 1987). In particular, the need to refill liquid nitrogen or helium regularly makes SQUIDs unattractive and expensive to operate in MT measurements that last from days to weeks or months, especially when located in remote localities. Nevertheless, owing to the shorter duration of measurements, SQUID magnetometers have been in use for surface or airborne time-domain CSEM measurements for 30 years (Kalberkamp et al. 1997; Chwala et al. 1999; Bick et al. 1999; Panaitov et al. 2002; Lee et al. 2002; Vallee et al. 2011; Asten and Duncan 2012; Smith 2014). For borehole AMT and BHEM measurements, SQUID sensors have the advantage that they are only 2 cm in side length. Miniaturising a cryostatic cooling system to fit into slim boreholes is a potentially promising option to obtain high-quality data that has not been explored yet.

We are not aware of previous field studies where MT electric fields recorded in boreholes were used to delineate ore deposits. To obtain localised measurements, bipoles with electrode separations of 25–50 m (Fig. 1) are an obvious option. To overcome ohmic losses in signal transmission to data loggers placed beside borehole openings, signals need to be preamplified at the sensor using a differential preamplifier. Alternatively, a single electrode may be deployed in the borehole and a reference electrode at the surface. Measuring at equally spaced depth levels and subtracting the fields recorded at adjacent depth levels then leads to transfer functions comparable to differential measurements at depth.

Owing to the pronounced skin effect in metal casing and the routine use of magnetic metals to produce metal casing, measurements of electric or magnetic fields in sections of boreholes with metal casing are meaningless. However, in hard-rock environments, it is common practice to install metal casings only in the shallow sections of boreholes that pass through the overlying sediments and weathering zone of the bedrock. In many regions of Sweden and Finland, for instance, the sedimentary cover and weathering zone are so thin that only the upper 10 m or so need to be cased. Depending on the instrumental set-up and the geological units drilled through, measurements at 50 m or more beneath the lower end of the metal casing are not affected by the metal casing. In loose sediments and sedimentary rocks, it is necessary to install a casing over the entire length of a borehole to prevent its collapse. However, in boreholes that are drilled, for instance, for hydrological
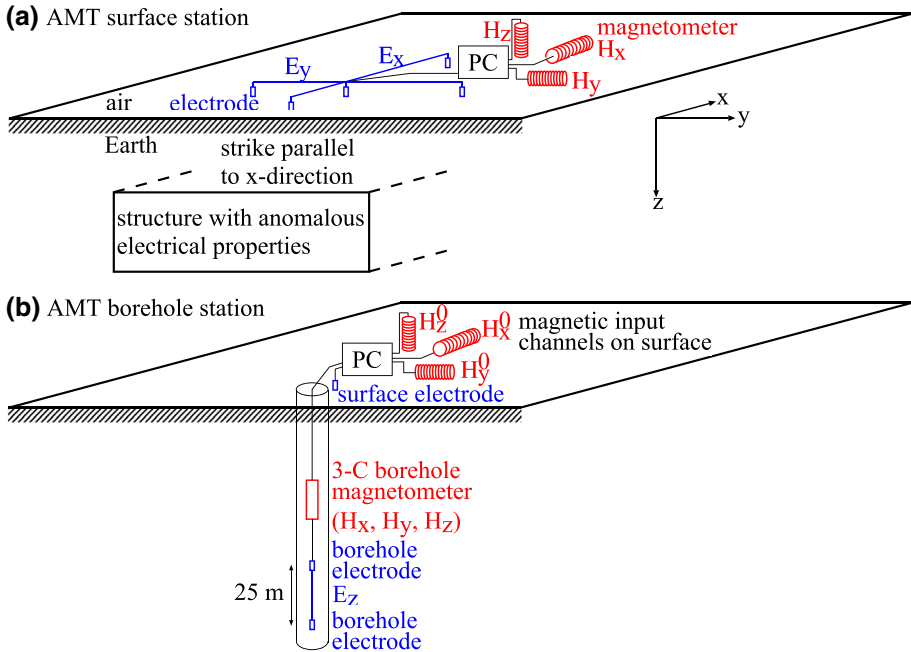
(a) AMT surface station

(b) AMT borehole station

Fig. 1 Instrumental set-ups for AMT measurements **a** on the surface using three induction coils to record horizontal (H_x and H_y) and vertical (H_z) magnetic fields and two 25–100-m-long grounded cables to record horizontal electric fields (E_x and E_y) and **b** in boreholes using a 3C magnetometer to record magnetic fields (H_x, H_y and H_z) at depth, three induction coils to record magnetic fields (H_x^0, H_y^0 and H_z^0) on the surface and a 25–50-m-long cable with electrodes on either end to record the axial electric field (E_z). **a** AMT surface station and **b** AMT borehole station

studies or in oilfields, slotted plastic casings are often installed. Since plastic casing does not lead to distortion of the electric and magnetic fields measured in boreholes, the methods described here can be directly applied.

1.5 Outline

In this paper, we present meaningful transfer functions between axial electric and magnetic fields measured in boreholes and surface magnetic fields, similar to West and Ward (1988) and Sasaki et al. (1992). Further, we study skin-effect transfer functions as defined by Spitzer (1993) and Schmucker et al. (2009). We elaborate on some particularities related to modelling borehole responses of 2D models using finite-difference approximations. Considering two synthetic examples of real ore deposits, we provide typical signal levels to aid future sensor development. Finally, we evaluate the improvements in model constraints that can be achieved by adding various types of MT borehole measurements to a set of standard MT surface measurements considering the same synthetic models as before. In this, particular emphasis is put to understand which improvements are possible to achieve in the lower parts of, and the structure beneath, conductive ore bodies. We present the first 2D inversion results involving TE-mode skin-effect transfer function and borehole vertical magnetic transfer function data.

2 Theory

2.1 2D Transfer Functions for Surface Measurements

From classical surface MT measurements over a 2D Earth (Fig. 1), transfer functions in the frequency domain are usually retrieved after time-series processing (involving Fourier transformation and robust stacking procedures) and rotation of the reference coordinate system such that the x-axis corresponds to the geoelectrical strike direction (Berdichevsky and Dmitriev 2008; Chave and Jones 2012). In this reference frame, the complex-valued and frequency-dependent impedance tensor $\mathbf{Z}$ relates the horizontal electric (E_x and E_y) and magnetic (H_x and H_y) fields as

$$\begin{bmatrix} E_x \\ E_y \end{bmatrix} = \begin{bmatrix} 0 & Z_{xy} \\ Z_{yx} & 0 \end{bmatrix} \begin{bmatrix} H_x \\ H_y \end{bmatrix}, \tag{1}$$

The impedance tensor element Z_{xy} is that of the transverse electric (TE) mode, where all current flow is directed along the strike direction. In contrast, the impedance tensor element Z_{yx} of the so-called transverse magnetic (TM) mode is related to current flowing in the plane perpendicular to the strike direction. These differences in the directions of current flow lead to pronounced differences in the resolving power for conductive and resistive targets. TE-mode responses are purely inductive in nature, and thus, they resolve predominantly conductive features (Berdichevsky et al. 1998; Pedersen and Engels 2005). In contrast, the current systems of the TM-mode charge the structures. Thus, TM-mode responses are sensitive to conductivity contrasts (Berdichevsky et al. 1998; Pedersen and Engels 2005).

Typically, the impedance tensor elements are converted to apparent resistivities ρ_a and phases ϕ

$$\rho_a^{xy} = \frac{1}{\omega\mu_0}|Z_{xy}|^2 \text{ and } \rho_a^{yx} = \frac{1}{\omega\mu_0}|Z_{yx}|^2, \tag{2}$$

$$\phi^{xy} = \arg(Z_{xy}) \text{ and } \phi^{yx} = \arg(Z_{yx}). \tag{3}$$

Additionally, in the TE-mode, the complex-valued and frequency-dependent vertical magnetic transfer function (VMTF) T_y relates the vertical and horizontal magnetic fields H_z and H_y, respectively, through

$$H_z = T_y \cdot H_y. \tag{4}$$

At the surface of a 1D Earth model, an obliquely incident plane-wave field is refracted towards the normal, which results from the large conductivity contrast between the air and the Earth. Under quasi-static conditions, this effect is so pronounced that the propagation in the strata of a 1D model is essentially in the vertical direction. Hence, $H_z = 0$ and $T_y = 0$, everywhere in the Earth and on the Earth's surface (Ward and Hohmann 1987).

2.2 2D Transfer Functions for Borehole Measurements

For borehole measurements, additional transfer functions of the TE and TM modes can be devised to relate field components measured in the borehole to others measured in the

borehole (borehole-to-borehole transfer functions) or at the surface (borehole-to-surface transfer functions).

Using 3C borehole magnetometers (Fig. 1), the complex-valued VMTF of the TE-mode can be computed. While only the vertical field component $H_z^{z=d}$ measured in a borehole at depth $z = d$ and normalised by a horizontal component $H_y^{z=0}$ measured at the Earth's surface (depth $z = 0$ m) was considered in a previous study (West and Ward 1988), we will also evaluate the benefits of a VMTF computed using borehole components. Hence, we consider both types of VMTF, i.e.

$$H_z^{z=d} = T_y \cdot H_y^{z=d}, \tag{5}$$

$$H_z^{z=d} = T_y^0 \cdot H_y^{z=0}. \tag{6}$$

For a 1D Earth and under quasi-static conditions, $H_z^{z=0}$ measured at the surface and $H_z^{z=d}$ measured in a borehole are identical to zero (see above). Hence, T_y and T_y^0 do not contain any information on the 1D resistivity distribution.

For the TM-mode and vertical boreholes, the vertical electric field $E_z^{z=d}$ (Fig. 1) can be related to the horizontal magnetic field measured at depth ($H_x^{z=d}$), the horizontal magnetic field measured at the Earth's surface ($H_x^{z=0}$) (e.g., West and Ward 1988; Sasaki et al. 1992) or to the horizontal electric field $E_y^{z=0}$ measured at the Earth's surface. Normalisation by the horizontal magnetic field H_x yields impedances or vertical electric transfer functions (VETF), i.e.

$$E_z^{z=d} = Z_{zx} \cdot H_x^{z=d}, \tag{7}$$

$$E_z^{z=d} = Z_{zx}^0 \cdot H_x^{z=0}, \tag{8}$$

whereas normalisation by the horizontal electric field leads to a transfer function S_{zy}^0 (Becken et al. 2008):

$$E_z^{z=d} = S_{zy}^0 \cdot E_y^{z=0}. \tag{9}$$

However, as $E_z = 0$ everywhere in a 1D Earth model under quasi-static conditions (Ward and Hohmann 1987), neither Z_{zx}, Z_{zx}^0 nor S_{zy}^0 hold information about the resistivity distribution of a 1D Earth. To avoid the influence of galvanic distortion effects possibly contained in electric fields measured on the surface (Jones 2012), we limit further consideration to the VETFs Z_{zx} and Z_{zx}^0.

With the purpose of reducing the effect of electric field distortion owing to small inhomogeneities, in the vertical gradient magnetometry (VGM) method (Jones 1983; Spitzer 1993; Schmucker et al. 2009), the electric fields E_x and E_y in Eq. 1 are replaced by vertical gradients of H_y and H_x, respectively, using Ampere's law. These vertical gradients are measured using borehole and surface sensors. As compared to the above transfer functions that involve either H_z or E_z at depth, VGM measurements are sensitive to layered structure. Two alternative definitions exist. Jones (1983) defined the 2D VGM transfer functions $\mathbf{V}^d$ of the TM and TE modes as

$$\mathbf{H}_h^{z=d} = \mathbf{V}^d \frac{\partial \mathbf{H}_h^{z=d}}{\partial z}, \tag{10}$$

$$\mathbf{V}^d = \begin{pmatrix} V_{xx}^d & 0 \\ 0 & V_{yy}^d \end{pmatrix}, \tag{11}$$

where $\mathbf{H}_h^{z=d} = \left(H_x^{z=d}, H_y^{z=d} \right)^{\mathrm{T}}$ is the vector of horizontal magnetic fields measured at depth $z = d$ and the gradient operator requires simultaneous measurements of the horizontal magnetic fields at closely spaced depth levels. Similar to the concept of the impedance tensor, Jones (1983) derived VGM apparent resistivities and phases

$$\rho_{a,xx}^{V^d} = \omega \mu_0 |V_{xx}^d|^2 \text{ and } \rho_{a,yy}^{V^d} = \omega \mu_0 |V_{yy}^d|^2, \tag{12}$$

$$\phi_{xx}^{V^d} = \arg\left(V_{xx}^d \right) \text{ and } \phi_{yy}^{V^d} = \arg\left(V_{yy}^d \right). \tag{13}$$

In contrast to Jones' point-wise definition, Spitzer (1993) and Schmucker et al. (2009) approximated $\frac{\partial H_x}{\partial z} \approx \frac{H_y^{z=d} - H_y^{z=0}}{d}$ and employed so-called skin-effect transfer functions (SETF) $\mathbf{A}^d$ between the horizontal magnetic fields at depth $z = d$ and at the Earth's surface $(z = 0\,\mathrm{m})$

$$\mathbf{H}_h^{z=d} = \mathbf{A}^d \mathbf{H}_h^{z=0}, \tag{14}$$

$$\mathbf{A}^d = \begin{pmatrix} A_{xx}^d & 0 \\ 0 & A_{yy}^d \end{pmatrix} \tag{15}$$

to approximate the impedance tensor.

Jones' (1983) VGM set-up necessitates simultaneous measurements of both horizontal magnetic field components at two adjacent depth levels. In practice, we would want to measure the vertical magnetic field component as well to retrieve the VMTF. Thus, two 3C magnetometers would have to be deployed simultaneously in the same borehole. Procurement of a 3C magnetometer is a substantial financial investment (at least for smaller exploration companies), and the prospect of losing two 3C magnetometers at the same time, because one gets stuck in the borehole, is certainly an undesirable financial risk. Hence, we consider only skin-effect transfer functions in the subsequent examples.

2.3 2D Forward and Inverse Modelling

The forward responses presented in the following sections were computed using the 2D finite-difference method following Weaver et al. (1985, 1986) and Kalscheuer et al. (2008). To compute the responses for sensors at depth, there are a few differences from the case with receivers at the Earth's surface. In the TE-mode, the computation of the auxiliary field components H_y and H_z from E_x requires no modification, other than allowing for non-vanishing conductivity above the sensor. In the TM-mode, the simulation of the axial electric field may require computation of the auxiliary field components E_y and E_z from H_x depending on borehole orientation. The computation of E_y at depth requires the computation of the full derivative of H_x in the vertical direction, because H_x no longer fulfils Laplace's equation above the node of interest as is the case for sensors at the Earth's

surface. Similarly, the computation of the auxiliary field component E_z depends on the horizontal (y-directed) derivative of H_x. As indicated above, we limit further consideration to the case of vertical boreholes. The results of the finite-difference method were verified by comparison with semi-analytic solutions (see the Appendix for details).

In the 2D smoothness-constrained least-squares inversion used here (Kalscheuer et al. 2010), the fit of the forward response of a model $\mathbf{m}$ to the field data is measured using the root-mean-square (RMS) misfit $RMS = \sqrt{\frac{1}{N_d}\|\mathbf{W}_d(\mathbf{d} - \mathbf{F}[\mathbf{m}])\|^2}$, where N_d is the number of data, $\mathbf{d}$ is a vector with N_d field measurements, $\mathbf{F}[\mathbf{m}]$ is the vector of N_d forward responses of $\mathbf{m}$, and $\mathbf{W}_d$ is a diagonal weighting matrix that contains the reciprocal standard deviations estimated for $\mathbf{d}$. Since the forward operator $\mathbf{F}[\mathbf{m}]$ is nonlinear in $\mathbf{m}$, a Taylor expansion up to first order (i.e. linearisation) involving the Jacobian matrix of partial derivatives is used to iteratively determine a model solution with minimum RMS misfit. The Jacobian matrix $\mathbf{J} = \{\partial F_i[\mathbf{m}]/\partial m_j\}_{\mathbf{m}=\mathbf{m}_k}$ is computed with respect to the model $\mathbf{m}_k$ at every iteration k and describes how the $i = 1, \ldots, N_d$ forward responses $F_i[\mathbf{m}_k]$ change for small perturbations in $j = 1, \ldots, N_m$ model parameters $m_{k,j}$. In comparison with measurements on the surface, additional entries for the two model cells just above a receiver node need to be included to simulate the Jacobian matrix of borehole measurements. In the subsequent inversion examples, all Jacobian matrices (sensitivities) were computed using the sensitivity equation method (McGillivray and Oldenburg 1990; Rodi and Mackie 2001; Kalscheuer et al. 2008). For a homogeneous half-space model and a blocky model with large resistivity contrasts (not shown), the computed sensitivities were verified using the computationally more expensive but easily implemented perturbation approach (McGillivray and Oldenburg 1990).

As model regularisation, smoothness constraints in the form of first- or second-order direct differences or derivatives of model resistivities are employed following Kalscheuer et al. (2010). In case of convergence problems, Marquardt–Levenberg damping is employed in addition to smoothness constraints. In this case, the Lagrange multiplier λ of the smoothness constraints is kept fixed, whereas the damping factor of the Marquardt–Levenberg constraints is varied automatically in every iteration using a line search to find the model that best fits the field data. A trial-and-error procedure is used to determine an optimal Lagrange multiplier λ such that an acceptable RMS misfit ($RMS \approx 1$) can be obtained.

2.4 Model Analysis

Using Kalscheuer et al.'s (2010) algorithm, we compute linearised model resolution and error estimates including smoothness constraints to evaluate how well our models are constrained by the data. Under certain assumptions (Kalscheuer et al. 2010), the model $\mathbf{m}_{k+1}$ computed at the $(k+1)$th iteration can be related to the unknown true model $\mathbf{m}_{\text{true}}$, an optional reference model $\mathbf{m}_r$ and the noise $\mathbf{n}$ contained in the data as

$$\mathbf{m}_{k+1} \approx \mathbf{R}_{\mathrm{M}}\mathbf{m}_{\text{true}} + (\mathbf{I} - \mathbf{R}_{\mathrm{M}})\mathbf{m}_r + \mathbf{J}_{\mathbf{W}}^{-g}\mathbf{W}_d\mathbf{n}, \qquad (16)$$

where $\mathbf{R}_{\mathrm{M}} = \mathbf{J}_{\mathbf{W}}^{-g}\mathbf{W}_d\mathbf{J}$ is the model resolution matrix, $\mathbf{J}_{\mathbf{W}}^{-g} = [\mathbf{J}^{\mathrm{T}}\mathbf{W}_d^{\mathrm{T}}\mathbf{W}_d\mathbf{J} + \lambda\mathbf{W}_m^{\mathrm{T}}\mathbf{W}_m]^{-1}\mathbf{J}^{\mathrm{T}}\mathbf{W}_d^{\mathrm{T}}$ is the generalised inverse, and the matrix $\mathbf{W}_m^{\mathrm{T}}\mathbf{W}_m = \alpha_y\partial_y^{\mathrm{T}}\partial_y + \alpha_z\partial_z^{\mathrm{T}}\partial_z$ contains the smoothness constraints enforced by horizontal and vertical gradient matrices ∂_y and ∂_z with weights α_y and α_z, respectively. The rows of the model resolution matrix describe how all parameters of the true model map into the individual parameters of the

estimated model. If $\mathbf{R}_M$ was the identity matrix $\mathbf{I}$, the estimated model would be perfectly resolved and not contain any contribution from the reference model. However, in all practical cases of 2D and 3D inversion, the model resolution matrix is singular, with non-vanishing values in the off-diagonal entries. For the well-resolved part of the model space, the rows of the model resolution matrix have well pronounced peaks centred on the corresponding model parameter. However, for the poorly resolved part of the model space, the rows have flat broader peaks spanning a large part of the model space, and they have positive and negative side lobes. Thus, the model resolution matrix $\mathbf{R}_M$ can be thought of as blurring filter through which we see the true model in the estimated model. For a given model parameter, the resolving kernel r_M is computed by scaling the entries of the corresponding row of the model resolution matrix $\mathbf{R}_M$ by the respective cell areas and, subsequently, we divide the entire resolving kernel by its maximum modulus, thus projecting the resolving kernel into the range of $[-1, 1]$. We compute the centres of resolution and horizontal and vertical resolution lengths according to Kalscheuer and Pedersen (2007) and indicate these using red crosses in the plots of our resolving kernels. Note that these centres of resolution and horizontal and vertical resolution lengths are appropriate representations of the resolving kernel only when it has a single main lobe. If the resolving kernel has multiple lobes, the centre of resolution is often estimated to be located outside the lobes.

The linearised model error estimates of the model $\mathbf{m}_{k+1}$ computed at the $(k+1)$th iteration of the inversion are the square roots of the diagonal entries of the model covariance matrix (Kalscheuer et al. 2010; Menke 2015)

$$[cov\,\mathbf{m}_{k+1}] \approx (\mathbf{I} - \mathbf{R}_M)[cov\,\mathbf{m}_r](\mathbf{I} - \mathbf{R}_M)^{\mathrm{T}} + \mathbf{J}_{\mathbf{W}}^{-g}\mathbf{J}_{\mathbf{W}}^{-g\,\mathrm{T}}, \tag{17}$$

where $[cov\,\mathbf{m}_r]$ is the covariance matrix of the optional reference model $\mathbf{m}_r$. In Eq. 17, the first and second terms describe how uncertainty in the reference model and the measurements, respectively, contributes to the uncertainty of the inversion model. Since Kalscheuer et al.'s (2010) algorithm employs logarithmic resistivities of the 2D cells, the errors on actual cell resistivities are factors f corresponding to resistivity ranges $[\rho/f, f\rho]$. Meju and Hutton (1992), Meju (1994), Kalscheuer and Pedersen (2007) and Kalscheuer et al. (2010) demonstrated that verification of linearised model error estimates using nonlinear most-squares inversion is generally desirable.

In smoothness-constrained schemes, $\mathbf{m}_r$ is typically a fixed vector. Hence, $[cov\,\mathbf{m}_r] = 0$ and $[cov\,\mathbf{m}_{k+1}] \approx \mathbf{J}_{\mathbf{W}}^{-g}\mathbf{J}_{\mathbf{W}}^{-g\,\mathrm{T}}$ is assumed. However, if $\mathbf{W}_m^{\mathrm{T}}\mathbf{W}_m$ is symmetric positive definite and uncertainty is associated with the reference model, the covariance matrix of the reference model is $[cov\,\mathbf{m}_r] = \left(\lambda\mathbf{W}_m^{\mathrm{T}}\mathbf{W}_m\right)^{-1}$ (e.g., Kalscheuer et al. 2010; Menke 2015). Substituting this expression into Eq. 17 and applying some matrix algebra yields

$$[cov\,\mathbf{m}_{k+1}] \approx \left[\mathbf{J}^{\mathrm{T}}\mathbf{W}_d^{\mathrm{T}}\mathbf{W}_d\mathbf{J} + \lambda\mathbf{W}_m^{\mathrm{T}}\mathbf{W}_m\right]^{-1}. \tag{18}$$

Since the most-squares error estimates are nonlinear equivalents of the square roots of the diagonal entries of Eq. 18 irrespective of the existence of $\left(\mathbf{W}_m^{\mathrm{T}}\mathbf{W}_m\right)^{-1}$ and variability in the reference model, most-squares inversion results need to be compared to the linearised error estimates in Eq. 18 (Kalscheuer et al. 2010). Furthermore, since error estimates computed using both terms in Eq. 17 (i.e. Eq. 18) are larger than those using only the second term representing data uncertainty, linearised model errors computed using Eq. 18 are the more conservative estimates.
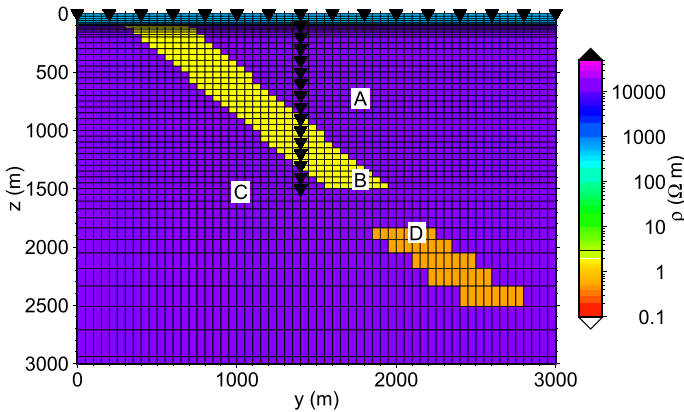
Fig. 2 2D model with two dipping mineralised zones of 1 Ωm and 0.5 Ωm embedded in a resistive background medium of 10,000 Ωm underneath a weathered surface layer of 100 Ωm. Sensor locations on the surface and in the borehole at $y = 1400$ m are indicated by black triangles

3 Synthetic Example 1: Conductive Mineralisations in Resistive Crystalline Bedrock

The true model of our first synthetic example shown in Fig. 2 represents an iron-ore mineralisation in the Kiruna area, northern Sweden. The mineralisation is dominated by magnetite and is located in an environment mainly composed of quartzitic sandstones and felsic volcanic rocks. Resistivity measurements have been performed on samples from the mineralisation and the host rocks, suggesting that the chosen model is realistic.

The model consists of two dipping mineralised zones of 1 Ωm (depth range $z = 100$–1500 m, distance along profile $y = 300$–1950 m) and 0.5 Ωm (depth range $z = 1840$–2620 m, distance along profile $y = 1900$–2800 m) embedded in resistive crystalline bedrock of 10,000 Ωm underneath a weathered surface layer of 100 Ωm and 100 m thickness. Surface receivers are evenly spaced at 200 m along a 3-km-long profile. At 1400 m along the line, a borehole with a maximum depth of 1500 m is positioned holding a total of 15 borehole sensors.

We have used identical finite-difference meshes in the forward and inverse modelling exercises. Note that the forward and inverse modelling code requires receivers to be located on the nodes of the grid. Thus, the joint simulation of signals at the surface and borehole receivers limits the ability of using strongly different meshes for forward and inverse modelling in both horizontal and vertical directions. Owing to the equidistant spacing of borehole receivers, we use a uniform vertical mesh discretisation for $z = 200$–1500 m depth. At shallower depth, the mesh discretisation is finer to account for the rapid resistivity transitions between the weathered overburden, the shallow mineral deposit and the resistive host rock. At greater depth, the thicknesses of the cells increase with a geometric progression factor of 1.15 to avoid excessive computation time. In the central part of the model, 73 nodes are spaced at 50 m distance in the horizontal direction. Including padding cells, the mesh has 114 and 92 cells in the horizontal and vertical direction, respectively. For simulation of TE-mode fields, 55 additional cells were used to discretise the air half space in the vertical direction. Owing to the pronounced 2D resistivity contrasts, a rather large number of cells in the air were required to avoid adverse

effects from scattering of the anomalous 2D fields at the boundaries of the computational domain.

3.1 Forward Responses, Signal Levels and Sensor Requirements

For the given receiver layout, we simulated surface and borehole measurements over a frequency range of 1 Hz–10 kHz using a total of 33 frequencies (i.e. 8 frequencies per decade). Note that the forward responses shown in Fig. 3 are for an $e^{+i\omega t}$ time dependence (where ω is angular frequency and t is time) and that all plots have frequency on the vertical axes, whereas the horizontal axes are profile distance y and depth z for surface and borehole measurements, respectively. The most striking features are the differences in variations of forward responses with receiver position. While the MT surface impedances (Z_{xy} and Z_{yx} in the upper two rows), the skin-effect transfer functions A_{xx}^d and A_{yy}^d and the vertical magnetic transfer function T_y^0 show comparatively smooth variation, the vertical electric transfer function Z_{zx}^0 exhibits much more abrupt changes with receiver position. The smooth variations of Z_{xy} and Z_{yx} are predominantly related to the fact that there are no lateral resistivity contrasts right at the surface due to the overburden weathered layer. In particular, Z_{yx} would have changed quite abruptly in such a case. Note that both Z_{zx}^0 and T_y^0 were simulated for input channels of the transfer functions (horizontal magnetic fields) at the surface. The real and imaginary parts of the VMTF T_y^0 attain values in a range of -1.0 to 1.0, comparable to measurements of T_y at the surface. In accordance with the contrast in conductivity along the borehole, the vertical electric field E_z, and with that the vertical electric transfer function Z_{zx}^0, changes abruptly with depth spanning a range of -2.0 to 2.0 V/A.

We have also considered vertical magnetic and electric transfer functions with horizontal magnetic field sensors at depth in boreholes (Z_{zx} and T_y). Since the sensors of both the output and input channels of these transfer functions traverse resistivity contrasts at depth simultaneously, these transfer functions vary more abruptly across resistivity contrasts than do Z_{zx}^0 and T_y^0 resulting in ranges of -6.0 to 6.0 V/A and -4.0 to 4.0, respectively, for our model (not shown). For inversion of such transfer functions, this leads to a higher degree of difficulty to converge to an acceptable inversion model given the discontinuous nature of the transfer functions competing with the applied smoothness constraints. In inversion tests using our synthetic data (not shown), about 200 iterations were required to obtain a sufficiently good inversion model (if convergence was obtained at all). In contrast, inversion of the T_y^0 and Z_{zx}^0 data required only several tens of iterations. Hence, we do not consider inversion of borehole T_y and Z_{zx} data any further. Note that this does not mean that we have excluded the horizontal magnetic fields at depth from the subsequently presented inversions. They are still considered as part of the skin-effect transfer functions A_{xx}^d and A_{yy}^d. Thus, borehole measurements of all three components of the magnetic field and the vertical component of the electric field contribute to the inversion models. The combination of A_{xx}^d, A_{yy}^d, Z_{zx}^0 and T_y^0 data should contain more information on the subsurface than Z_{zx} and T_y data. We cannot prove this using inversion though because of the convergence problems associated with Z_{zx} and T_y. For noise-free data, Z_{zx} and T_y could be obtained by division of Z_{zx}^0 and T_y^0 through A_{xx}^d and A_{yy}^d, respectively. For noisy data, owing to different results in data processing, e.g., coherence thresholding, divisions would not yield results identical to Z_{zx} and T_y. Nevertheless, adding Z_{zx} and T_y to the set of
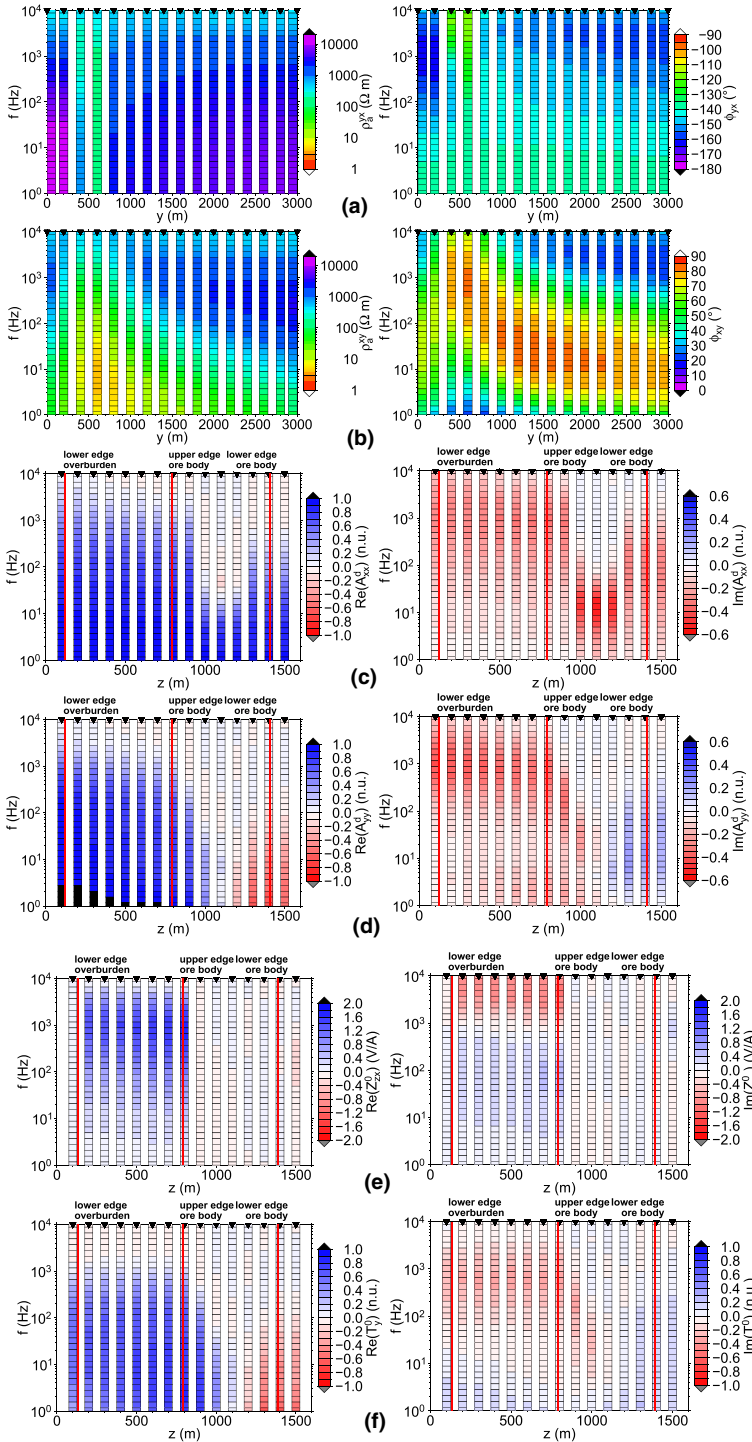
◀ **Fig. 3** AMT forward responses of the model shown in Fig. 2 for **a** TM-mode surface impedance Z_{yx}, **b** TE-mode surface impedance Z_{xy}, **c** TM-mode borehole skin-effect transfer function A_{xx}^d, **d** TE-mode borehole skin-effect transfer function A_{yy}^d, **e** TM-mode borehole vertical electric transfer function Z_{zx}^0 and **f** TE-mode borehole vertical magnetic transfer function T_y^0. Forward responses were computed for the AMT frequency range of 10 kHz–1 Hz. Z_{zx}^0 and T_y^0 are computed using magnetic fields at the surface as input channels. In **c**–**f**, red lines mark structural boundaries traversed by the borehole

borehole data employed in the subsequently presented inversions would add at least partly redundant information.

The sources of AMT signals are electric discharges through thunderstorms distributed over the globe, but predominantly occurring in tropical regions (Vozoff 1991; Brasse and Rath 1997; Garcia and Jones 2002; Sternberg 2010). The generated EM fields propagate through the lossy waveguide defined by the surfaces of the Earth and the lower ionosphere, experiencing damping at both surfaces. There is considerable variability in the damping experienced in the lower ionosphere, which directly depends on the strength of photo-ionisation through solar radiation and, thus, varies with latitude, with the time of the day, with the season and with the eleven-year sunspot cycle. Furthermore, signal levels change with the diurnal and seasonal variations in lightning activity. Since the damping in the lower ionosphere depends on frequency, time and location, typical AMT spectral signal strengths of the horizontal magnetic flux at the Earth's surface vary from about 10^0–10^6 fT$/\sqrt{\text{Hz}}$ at 1 Hz to a low 10^{-3}–10^4 fT$/\sqrt{\text{Hz}}$ at 1000–2000 Hz in the AMT dead band (where signal attenuation due to propagation in the Earth-ionosphere waveguide is enhanced by the ionospheric D-layer on the day-side of the Earth, e.g., Brasse and Rath 1997), and increase to still relatively low values of 10^{-2}–10^4 fT$/\sqrt{\text{Hz}}$ at 10,000 Hz (Vozoff 1991; Brasse and Rath 1997; Sternberg 2010). Nevertheless, the actual range of amplitude variation can be different, depending in addition to the factors mentioned above on observation length. For a study of the amplitudes in the AMT dead band at frequencies of 1000 and 2000 Hz for two locations in Canada and Germany, Garcia and Jones (2002) reported a range of 10^{-1}–10^6 fT$/\sqrt{\text{Hz}}$. Typically, the largest AMT magnetic field amplitudes are observed around midnight during the summer months. Modern induction coils and SQUID magnetometers for surface measurements have spectral noise levels as good as $10^{1.5}$–$10^{2.5}$ fT$/\sqrt{\text{Hz}}$ at 1 Hz, $10^{-0.5}$–$10^{0.5}$ fT$/\sqrt{\text{Hz}}$ at 1000–2000 Hz and $10^{-0.7}$–$10^{0.5}$ fT$/\sqrt{\text{Hz}}$ at ∼ 10,000 Hz (Ferguson 2012), meaning that the lower-amplitude AMT signals during daytime may be difficult to detect and emphasising the requirement for AMT measurements to be performed at night-time. Since the borehole transfer functions employed here use surface measurements as direct reference, we evaluate signal levels at depth based directly on the skin-effect transfer functions. The real part of the skin-effect transfer function A_{xx}^d in Fig. 3 varies from 1.0 at the lowest frequency of 1 Hz to negative values of − 0.2 at the highest frequency of 10 kHz. However, the real part of A_{yy}^d exhibits more complicated behaviour. While the absolute values of $\text{Re}\left(A_{yy}^d\right)$ are below 0.2 at 10 kHz, at 1 Hz $\text{Re}\left(A_{yy}^d\right)$ decreases from about 1.0 at shallow depth to − 0.6 in the lower part of the borehole. In the resistor overlying the dipping ore body, the imaginary parts attain values as low as ∼ − 0.4 at 1 kHz, whereas absolute values of 0.4–0.5 occur at lower frequencies inside and below the ore body. As expected, the skin effect is strongest at the highest frequencies and inside the conductive ore body. To obtain measurements of very high quality, the noise characteristics of borehole sensors at the highest frequencies would ideally have to be four to five times better than those of surface sensors.

Nevertheless, borehole sensors with noise characteristics comparable to those of modern surface sensors would be sufficient in many practical situations. One may argue that improved sensor characteristics are required to record skin-effect transfer functions close to zero, such as at high frequency inside the conductor. However, at such low signal levels, ambient noise or noise induced by ground water flow that moves the sensor inside the borehole is likely to be more dominant than sensor noise. Thus, reduced sensor noise might make little difference close to zero transitions. As an aside, noise induced by ground water flow can be eliminated by fastening the sensor against the borehole wall. However, this may damage the borehole in weaker sections and borehole owners may have a restrictive policy to fastening sensors.

3.2 2D Inversions

Prior to inversion, the synthetic data were contaminated with Gaussian noise. Random numbers were drawn from a uniform distribution in [0, 1], subjected to a shuffling procedure to eliminate possible sequential correlations in the series of random numbers provided by the computer system (Press et al. 1991) and subsequently converted to samples from Gaussian (normal) distributions with zero mean (to simulate bias-free data) and the desired standard deviations using the Box–Muller algorithm (Box and Muller 1958). For the surface TE-mode and TM-mode impedances, noise corresponding to 2.5% relative error was added to the impedance tensor elements. Assuming that the limited physical size of the magnetic borehole sensors would lead to higher noise levels than for the surface measurements, we contaminated the synthetic borehole responses for A_{xx}^d and A_{yy}^d with Gaussian noise corresponding to 0.05 absolute error. Since the real and imaginary parts of A_{xx}^d and A_{yy}^d may vary between -1 and 1, this absolute noise level corresponds to $> 5\%$ relative noise. Since borehole Z_{zx}^0 and T_y^0 data do not have as clearly defined upper amplitude limits as surface measurements of T_y (typically less than 1.0), but rather change based on resistivity contrasts at depth, we assumed a combination of absolute errors (0.05 V/A on Z_{zx}^0 and 0.05 on T_y^0) and relative errors (5% in either case). While we have taken a conservative attitude regarding noise levels in borehole measurements, we note that borehole conditions (e.g., absence of wind induced noise, larger distance to anthropogenic noise sources) may be rather benign compared to conditions on the surface leading to data with little noise. In the inversions, we set the standard deviations of the data to the error levels employed for noise contamination.

The simultaneous zero transitions of the real and imaginary parts of the skin-effect transfer functions lead to a higher degree of instability in the skin-effect transfer functions than for the surface impedances. Since the vertical electric and magnetic fields are zero in a 1D Earth and contain only little information on the resistivity distribution of a layered background medium, inversion of Z_{zx}^0 and T_y^0 transfer function data is inherently more unstable and prone to introducing model artefacts than the inversion of surface impedance data or skin-effect transfer functions $\mathbf{A}^d$. Hence, an inversion strategy needed to be developed to exploit the $\mathbf{A}^d$, Z_{zx}^0 and T_y^0 borehole data to the maximum extent. We found that surface and borehole data can be inverted in a stable and reliable manner using a three-step procedure:

1. Only the surface measurements are inverted using Occam or damped Occam regularisation.

2. Surface impedances and skin-effect transfer functions are jointly inverted using a damped Occam regularisation and the final inversion model of the surface data as the initial model.

3. Surface impedances, skin-effect transfer functions, and borehole vertical electrical and magnetic transfer functions are jointly inverted using a damped Occam regularisation and the final inversion model of the surface impedances and skin-effect transfer function data as the initial model.

Introducing additional damping in the second and third steps sets the inversion model retrieved in the previous step as an initial reference model, and modifications of the model are at the same time kept to the minimum and in fulfilment of the additional constraints provided by the borehole data. If vertical electrical and/or magnetic transfer functions are the only available borehole data, the procedure is condensed to a two-step procedure where the first step is the same as in the three-step procedure. Note that similar stepwise inversion strategies are typically applied in the inversion of surface impedance and VMTF data (e.g., Weckmann et al. 2007; Rao et al. 2014). When the number of complementary data sets entering into the inversion is increased, such as in our three-step procedure, it can be expected that the acceptable model space is reduced and the model becomes better constrained by the data. Therefore, the Lagrange multiplier that determines the strength of the model smoothness constraints may be reduced in the last two steps of our three-step procedure to reach an acceptable data fit.

For this first synthetic example, all of the subsequently presented inversion models were computed using a two-to-one weighting of horizontal to vertical smoothness constraints (i.e. by setting $\alpha_y = 2$ and $\alpha_z = 1$). Other weights, such as a one-to-one weighting using a correspondingly increased Lagrange multiplier λ, led to increased RMS misfits.

3.2.1 Inversion of Surface AMT Data

For the inversion of the surface impedance data, we used a homogeneous half space with a resistivity of $1000\,\Omega$m as the initial model. The inversion model in Fig. 4a (RMS = 1.02 after 17 iterations using Occam inversion followed by 21 iterations with additional Marquardt–Levenberg damping) demonstrates the limited resolving power of surface measurements. While the hanging wall of the shallow ore body is relatively well resolved, the foot wall is smeared out towards depth and cannot be imaged clearly. From the inversion model, one would not conclude anything about the existence of the deep ore body. We performed two further tests. First, we extended the profile by 600 m to either side (not shown), but this did not improve model constraints for the resistive host unit below the shallow ore body or for the deep ore body. Second, we included VMTF data for the stations on the surface in the inversion. Starting with the model in Fig. 4a as the initial model, this led to an initial RMS misfit of 1.04 for the combined data set of TM-mode impedances, TE-mode impedances and VMTFs. Within four iterations, the RMS misfit was reduced to 0.98. Though the inversion model of this iteration (not shown) had a marginally more focused shallow ore body, the model improvement is insignificant when compared to the subsequently described inversions that included borehole measurements.

3.2.2 Inversion of Surface and Borehole AMT Data

As compared to the inversion model of surface data, the joint inversion models of surface and borehole AMT measurements in Fig. 4b (A_{xx}^d and A_{yy}^d added; RMS = 1.01; 5 iterations
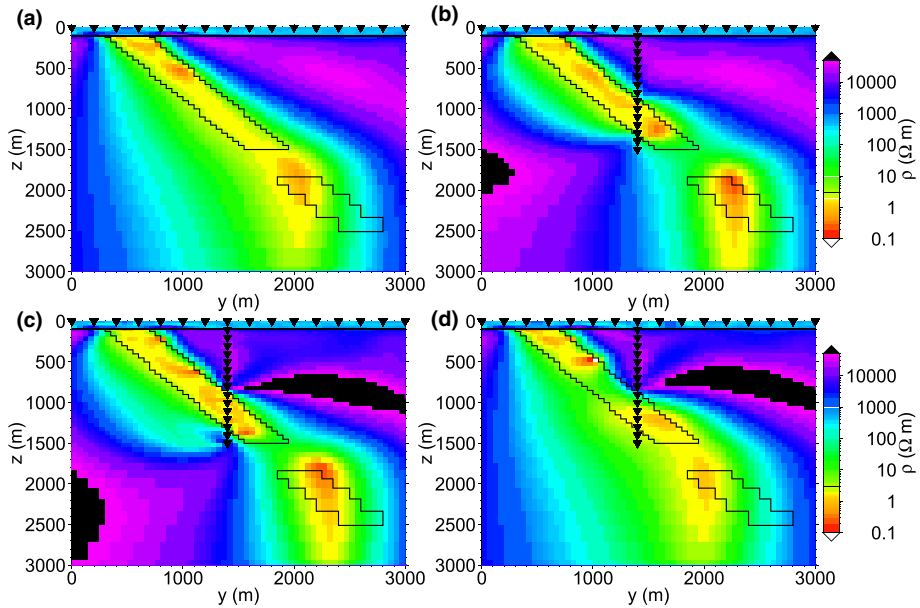
Fig. 4 Inversion models of synthetic data for the true model in Fig. 2: inversions of **a** TM- and TE-mode surface impedances (Z_{yx} and Z_{xy}; Lagrange multiplier $\lambda = 10^{0.7}$; RMS = 1.02), **b** TM- and TE-mode surface impedances and TM- and TE-mode borehole skin-effect transfer functions (Z_{yx}, Z_{xy}, A_{xx}^d and A_{yy}^d; Lagrange multiplier $\lambda = 10^{0.7}$; RMS = 1.01), **a** TM- and TE-mode surface impedances, TM- and TE-mode borehole skin-effect transfer functions, TM-mode borehole vertical electric transfer functions and TE-mode borehole vertical magnetic transfer functions (Z_{yx}, Z_{xy}, A_{xx}^d, A_{yy}^d, Z_{zx}^0 and T_y^0; Lagrange multiplier $\lambda = 10^{0.5}$; RMS = 1.02), **d** TM- and TE-mode surface impedances and TM-mode borehole vertical electric transfer functions (Z_{yx}, Z_{xy} and Z_{zx}^0; Lagrange multiplier $\lambda = 10^{0.7}$; RMS = 1.09). Black outlines indicate structural boundaries of the true model in Fig. 2

using Occam inversion followed by 32 iterations with additional Marquardt–Levenberg damping) and Fig. 4c (A_{xx}^d, A_{yy}^d, Z_{zx}^0 and T_y^0 added; RMS = 1.02; 13 iterations using Occam inversion followed by 200 iterations with additional Marquardt–Levenberg damping) show clearly improved resolution at depth along the hanging and foot walls of the shallow ore body. Also, the shallow ore body itself is much better delineated in the vicinity of the borehole. For the given model and experimental geometry, the data do not constrain the deep ore body well, but in the inversion models in Fig. 4b, c the upper edge appears to be partly resolved.

3.2.3 Inversion of Surface and Borehole Z_{zx}^0 AMT Data

At present, 3C magnetometers suitable for AMT borehole measurements are not available. In fact, we are not even aware of a suitable sensor for the axial magnetic field. Hence, one has to resort to recording axial electrical fields only in boreholes. Owing to the lacking sensitivity of AMT Z_{zx}^0 data to the resistivity of layered background media, we found the inversion of AMT surface impedances and borehole Z_{zx}^0 data starting from the model of the AMT surface impedances to be a difficult process. In an initial Occam inversion, the RMS misfit was reduced from 7.31 (for the model computed from the surface impedances) to

2.33 within 72 iterations. Subsequently, the damped Occam inversion required 22 iterations to reduce the RMS misfit from 2.33 to 1.11. A total of 89 damped Occam iterations were required to obtain RMS = 1.09, but this did not improve the model any further. As compared to the inversion model of surface AMT data (Fig. 4a), the inversion model of surface impedance and borehole Z_{zx}^0 data presented in Fig. 4d shows improvement solely for the resistivity distribution along the borehole but not for the resistivity distribution at more than ~ 400 m laterally off the borehole or below the borehole. It turned out that fitting the Z_{zx}^0 data of the deepest station immediately beneath the shallow ore body did not succeed (RMS = 2.76 for the Z_{zx}^0 data of that station), which may be one reason for not improving the model at depth below the borehole. The limited sensitivity of the vertical electric transfer function data (Z_{zx}^0) for structures at more than ~ 400 m laterally off the borehole is reminiscent of the limited sensitivity of DHMMR and surface MMR data to structures at similar distance (e.g., Asten 1988; Bishop et al. 1997; Chen et al. 2002).

3.3 Model Resolution and Error Analysis

In Figs. 5, 6, 7 and 8, we present model resolving kernels from a linearised analysis (Kalscheuer et al. 2010) for the cells marked A-D in Fig. 2 of the models in Fig. 4. For a meaningful comparison of resolution properties, cells A, B and C have equal horizontal
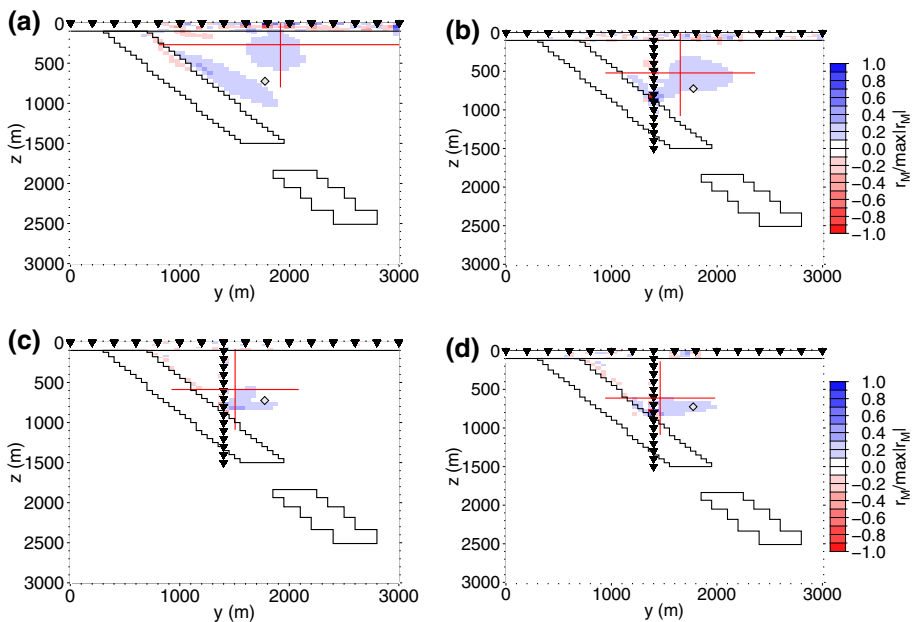

Fig. 5 Resolving kernels r_M for cell A (marked by white diamond, cf. Fig. 2) of models in Fig. 4 inverted from **a** TM- and TE-mode surface impedances (Z_{yx} and Z_{xy}), **b** TM- and TE-mode surface impedances and TM- and TE-mode skin-effect transfer functions (Z_{yx}, Z_{xy}, A_{xx}^d and A_{yy}^d), **c** TM- and TE-mode surface impedances, TM- and TE-mode skin-effect transfer functions, TM-mode borehole vertical electric transfer functions and TE-mode borehole vertical magnetic transfer functions (Z_{yx}, Z_{xy}, A_{xx}^d, A_{yy}^d, Z_{zx}^0 and T_y^0), **d** TM- and TE-mode surface impedances and TM-mode vertical electric transfer functions (Z_{yx}, Z_{xy} and Z_{zx}^0). Red lines and their crossing points represent resolution lengths and centres estimated using Kalscheuer and Pedersen's (2007) method
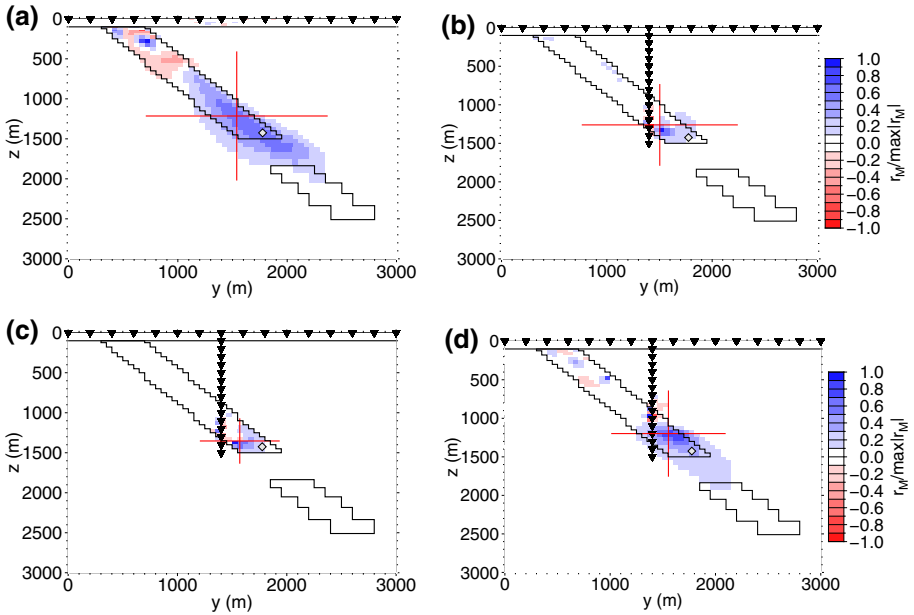
Fig. 6 Resolving kernels r_M for cell B (cf. Fig. 2) of models in Fig. 4 from inversions of the same data sets as in Fig. 5
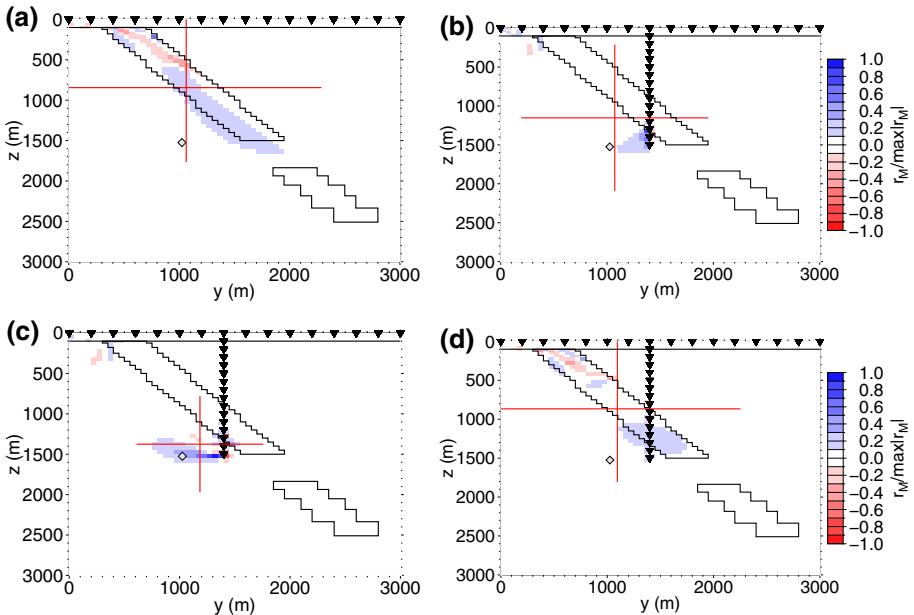

Fig. 7 Resolving kernels r_M for cell C (cf. Fig. 2) of inversion models in Fig. 4 from inversions of the same data sets as in Fig. 5
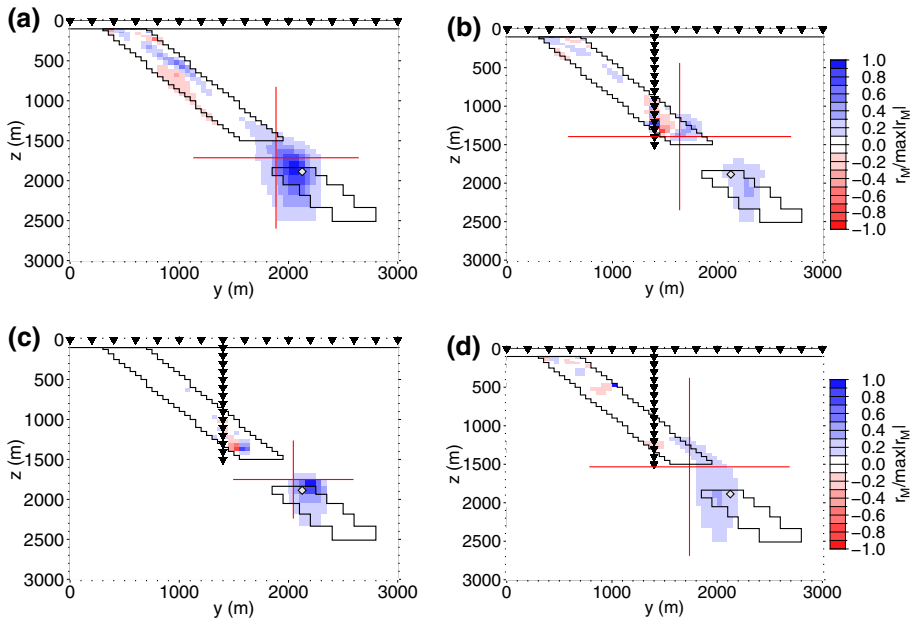
Fig. 8 Resolving kernels r_M for cell D (cf. Fig. 2) of inversion models in Fig. 4 from inversions of the same data sets as in Fig. 5

distance from the borehole. For cell A above the hanging wall of the shallow deposit and to the right of the borehole, the resolving kernel for the model derived from the surface impedances is unfocused and contains many nonzero entries from near surface cells, the resistive unit above the hanging wall and the shallow ore body (Fig. 5a). Successive inclusion of skin-effect and borehole vertical electric and magnetic transfer functions leads to successively stronger focusing of the resolving kernel in the vicinity of cell A (Fig. 5b, c). However, in no case is the resolving kernel centred on cell A.

For cell B in the lower part of the shallow ore body, the resolving kernel of the model derived from surface impedances (Fig. 6a) suggests that the estimated parameter is a gross average over much of the shallow ore body. Addition of borehole measurements to the inverted data set leads to resolving kernels that are highly focused (with a spread of no more than 300 m) and the centre of resolution is offset by a little less than 250 m from the cell under investigation (Fig. 6b, c). Even adding just Z_{zx}^0 data leads to significant improvement in model resolution (Fig. 6d).

For cell C to the left of and below the shallow ore body, the resolving kernel for the model computed from surface impedances (Fig. 7a) has a large spread over cells of and immediately beneath the shallow ore body, and demonstrates that the estimated model parameter (cf. Fig. 4a) is not at all constrained by the data. Adding borehole measurements leads to a discernible improvement with the resolving kernels (Fig. 7b, c) now having their main lobes in the vicinity of cell C. However, the resolving kernels still have comparatively large spreads (~ 500 m) and are, as mentioned above, not centred on the cell. While the centre of cell C is at 375 m lateral distance from the borehole, cells at a comparable depth level and closer proximity to the borehole have better resolution (not shown). Unlike cell B and as compared to the model computed from surface impedances only, addition of

Table 1 Model errors f for cells A–D (cf. Fig. 2)

Data		Cell A	Cell B	Cell C	Cell D
Surface impedances	Resolving kernel	Fig. 5a	Fig. 6a	Fig. 7a	Fig. 8a
	Factor $f_{[covd]}$	1.12	1.14	1.10	1.13
	Factor f_{tot}	1.90	1.86	2.01	1.74
Surface impedances and borehole SETF	Resolving kernel	Fig. 5b	Fig. 6b	Fig. 7b	Fig. 8b
	Factor $f_{[covd]}$	1.14	1.15	1.15	1.13
	Factor f_{tot}	1.85	1.83	1.88	1.83
Surface impedances, borehole SETF, borehole VETF and borehole VMTF	Resolving kernel	Fig. 5c	Fig. 6c	Fig. 7c	Fig. 8c
	Factor $f_{[covd]}$	1.12	1.20	1.20	1.20
	Factor f_{tot}	2.07	2.08	2.04	1.92
Surface impedances and borehole VETF	Resolving kernel	Fig. 5d	Fig. 6d	Fig. 7d	Fig. 8d
	Factor $f_{[covd]}$	1.12	1.11	1.11	1.12
	Factor f_{tot}	1.76	1.83	2.00	1.78

Linearised error factors $f_{[covd]}$ and f_{tot} were computed from the last term and both terms of eq. (17), respectively. Parameter uncertainties correspond to value ranges of ρ/f to $f \cdot \rho$, which would define 68% confidence intervals, if the inversion problem was linear. *SETF* skin-effect transfer functions, *VETF* vertical electric transfer functions, *VMTF* vertical magnetic transfer functions

just Z_{zx}^0 borehole data may only lead to a marginally better resolved resistivity of cell C (Fig. 7d).

For cell D in the deep ore body, neither the resolving kernel of the model derived from the surface impedances (Fig. 8a) nor the resolving kernel of the model derived from the surface impedances and vertical electric transfer functions (Fig. 8d) suggest that the parameter is particularly well constrained by the data. However, addition of the skin-effect transfer functions focuses one of the two main lobes of the resolving kernel on the upper part of the deep ore body suggesting that this part of the structure is at least partly constrained by the combined data set.

The model error factors f from a linearised analysis (Kalscheuer et al. 2010) presented in Table 1 do not exceed 1.20 for the more traditionally employed expression related to data uncertainty only (second term in Eq. 17) and 2.08 for the complete expression including the terms related to uncertainty of both model constraints and data (both terms of Eq. 17). These maximal error factors correspond to 68% confidence intervals of $[\frac{1}{1.20}\rho, 1.20\rho]$ or $[\frac{1}{2.08}\rho, 2.08\rho]$ depending on which expression is used. In the model from joint inversion of AMT data collected on the surface and in the borehole (Fig. 4c), the resistivities of cells A–D are closer to the resistivities of the true model in Fig. 2 than in the other inversion models. However, for the cells investigated, the linearised uncertainty ranges of the resistivities from inversion do not include the true resistivities. At least for cells A and D, the true cell resistivities fall into the 95% confidence intervals of $[\frac{1}{f^2}\rho, f^2\rho]$ for the error factors f related to uncertainty of both model constraints and data. Cells B and C are located in model regions where the resistivities smoothly transition between low and high values. For cells closer to the borehole, the constraints delivered by the data are stronger, and the confidence intervals come closer to, or include, the true resistivities. In combination with the resolving kernels in Figs. 5, 6, 7 and 8 for the model in Fig. 4c, one can conclude the resistivity of cell B is well constrained by the data, and the resistivities of

cells A, C and D are moderately well constrained by the data. As is evident from the resolving kernels of all investigated cells, the joint inversion models in Fig. 4b, c are much better constrained than the models from inversion of surface data alone (Fig. 4a) and from joint inversion of surface and Z_{zx}^0 borehole data (Fig. 4d). By adding Z_{zx}^0 borehole data to the surface impedance data, we can constrain the resistivities of cells A and B better (cf. Fig. 4a, d). This result confirms that the Z_{zx}^0 borehole data are predominantly sensitive to structures in the vicinity of the borehole, whereas the skin-effect transfer functions add constraints for structures both below and to the sides of the borehole.

We found that the smoothness-constrained most-squares inversion by Kalscheuer et al. (2010) worked unreliably when data sets including borehole measurements were considered. Hence, we do not present the results of the most-squares inversion. For the data set consisting of surface impedances and skin-effect transfer functions, all most-squares errors were lower than the linearised ones, which we do not believe is correct. For the data set consisting of surface impedances and vertical electric transfer functions, the model parameter deviation corresponding to the overall target misfit computed using a tentative damping factor already in the first iteration was consistently larger than the cumulative model parameter deviation in the last iteration. Most likely, these seemingly wrong results are a direct consequence of the general difficulties to make inversions that include borehole data sets converge optimally.

4 Synthetic Example 2: Moderately Conductive Mineralisations in a Sedimentary Succession

Our second synthetic example is based on previous geological, geophysical and petrophysical knowledge of two zinc mineralisations and their surroundings in Ireland. The example is designed to test the additional information that may be possible to gain from
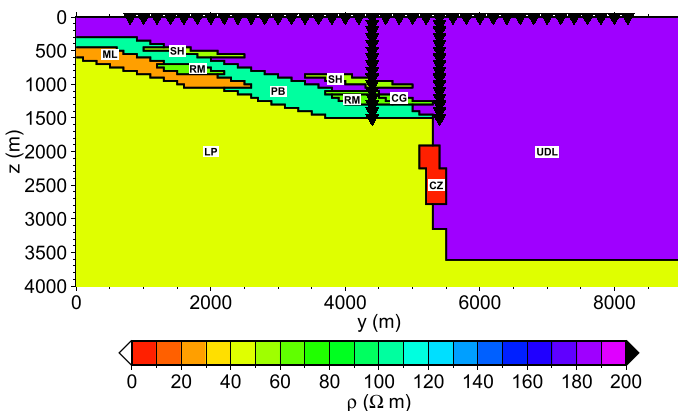

Fig. 9 2D model with three mineralised zones (*RM* red mineralisations: 64 Ωm and *CZ* conceptual copper zone: 3 Ωm) embedded in a moderately resistive sedimentary succession (*UDL* upper dark limestones: 180 Ωm, *CG* conglomerate: 68 Ωm, *PB* pale beds: 100 Ωm, *ML* muddy limestone: 25 Ωm and *LP* lower Palaeozoic units: 45 Ωm). Red mineralisations are believed to be overlain by syngenetic halos (*SH*) of ∼ 50 Ωm. Sensor locations on the surface and in the boreholes are indicated by black triangles

Fig. 10 AMT and BBMT forward responses of the model shown in Fig. 9 for **a** TM-mode surface ▶ impedance Z_{yx}, **b** TE-mode surface impedance Z_{xy}, **c** TM-mode borehole skin-effect transfer function A_{xx}^d, **d** TE-mode borehole skin-effect transfer function A_{yy}^d, **e** TM-mode borehole vertical electric transfer function Z_{zx}^0 and **f** TE-mode borehole vertical magnetic transfer function T_y^0. Forward responses were computed for a combined AMT and BBMT frequency range of 10 kHz–0.001 Hz. Responses in panels **c**–**f** are for the borehole at $y = 4400$ m along the profile; red lines indicate structural boundaries in the true model. Z_{zx}^0 and T_y^0 were computed using magnetic fields at ground surface as input channels

down-hole AMT and BBMT measurements in search for an, as yet, undiscovered conceptual deeper target related to a fault zone. The fault zone, interpreted from extant 2D seismic data, is located beneath the moderately conductive cover rocks.

In this example, the true model (Fig. 9) consists of a succession of sedimentary layers that become more conductive with depth (resistivity decreases from 180 Ωm to 45 Ωm) and three mineralisations zones (two "red mineralisations", i.e. zinc mineralisations, of 64 Ωm at 700–1300 m depth and a conceptual copper zone of 3 Ωm at 1850–2850 m depth). Since the resistivity contrasts are much smaller than in the first example (Fig. 2), it can be expected that the responses in the vertical magnetic and electric transfer function Z_{zx} and T_y, respectively, are smaller in amplitude. Further, since the background resistivity predominantly decreases with depth, it can be expected that surface data alone can constrain the model rather well (e.g., Bedrosian 2007; Kalscheuer and Pedersen 2007). In our experimental set-up, 38 surface receivers are evenly distributed along the profile at a station spacing of 200 m with the first receiver at 800 m along the line. Two 1500-m-deep boreholes are located at 4400 and 5400 m along the line penetrating one of the red mineralisations and ending 350 m above the conceptual copper zone, respectively. Using a sensor spacing of 100 m, there are 15 depth levels with borehole receivers.

As for the first example, we have used identical finite-difference meshes for forward and inverse modelling. In the central part of the mesh, we used two cells in horizontal direction between adjacent receivers. The equidistant spacing of borehole receivers resulted in uniform vertical mesh discretisation of 50 m at $z = 100$–1500 m. At shallower depth towards the air–Earth interface, the mesh discretisation is finer to facilitate accurate numerical modelling (the lowest cell thickness of 3.2 m is at $z = 0$ m). At greater depth, the cell thickness increases with a geometric progression factor of 1.25. Including padding cells, the mesh has 155 and 64 cells in the horizontal and vertical directions, respectively. For simulation of TE-mode fields in the air half space, additional 42 cells were used in the vertical direction to guarantee sufficient amplitude reduction in the anomalous fields towards the outer mesh boundaries through geometric spreading.

4.1 Forward Responses and Signal Levels

For the model and station locations in Fig. 9, we have simulated transfer functions for a combination of 57 AMT and BBMT frequencies from 10 kHz–0.001 Hz (Fig. 10). We included lower-frequency BBMT signals, because a comparison of inverse simulations based on AMT signals only and a combination of AMT and BBMT signals demonstrated that the conductive unit LP at depth and the conceptual copper zone are better constrained when BBMT transfer functions are included (see below). Induction coils are perfectly suitable for recording signals of frequencies as low as 0.001 Hz. In practice, AMT stations with induction coils are deployed over night such that measurements of the frequency range simulated by us are collected.
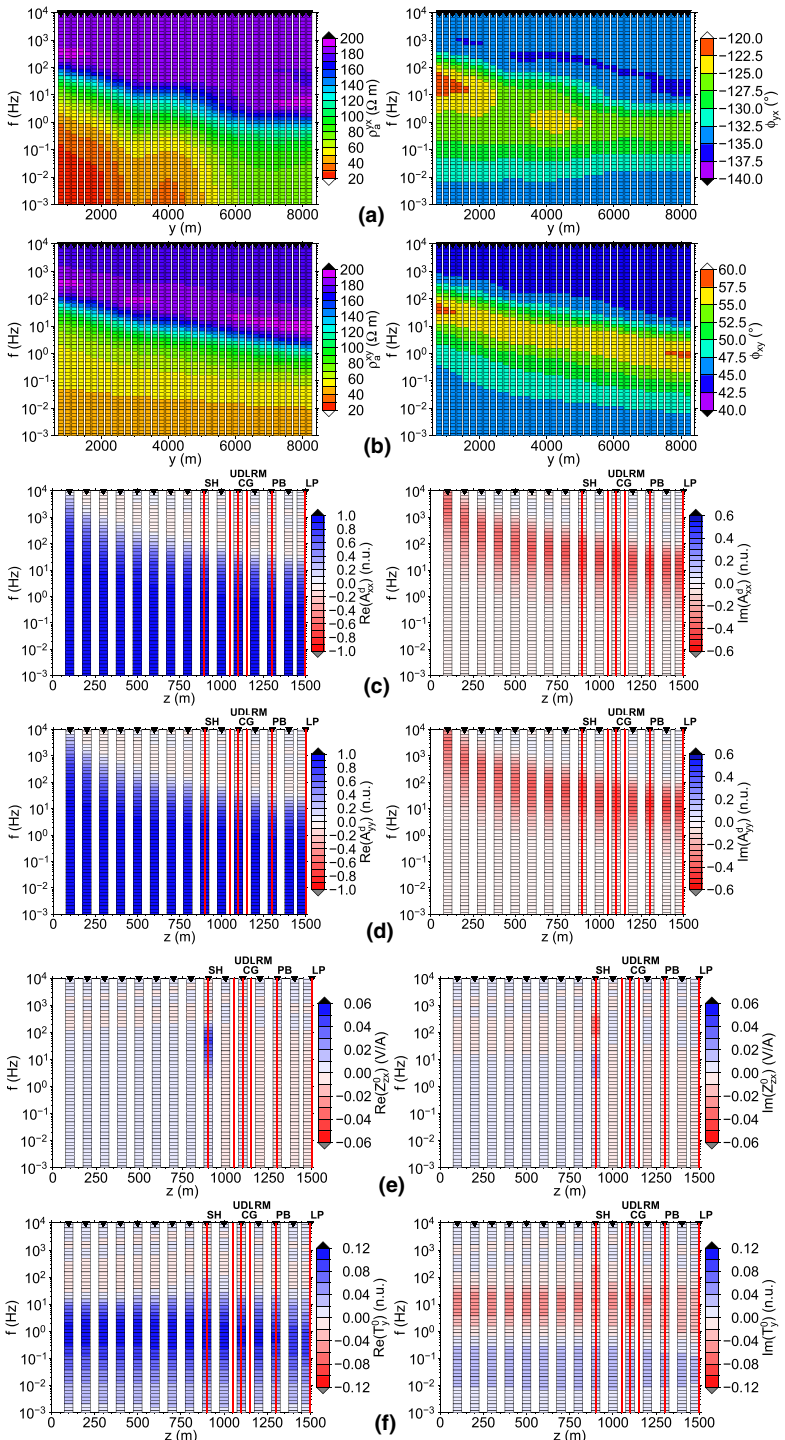
Fig. 11 Inversion models of synthetic data for the true model in Fig. 9: inversions of **a** TM- and TE-mode ▶ surface impedances (Z_{yx} and Z_{xy}; Lagrange multiplier $\lambda = 10^{2.4}$; RMS = 1.02), **b** TM- and TE-mode surface impedances and TM- and TE-mode borehole skin-effect transfer functions (Z_{yx}, Z_{xy}, A_{xx}^d and A_{yy}^d; Lagrange multiplier $\lambda = 10^{2.0}$; RMS = 1.00), **c** TM- and TE-mode surface impedances, TM- and TE-mode skin-effect transfer functions, TM-mode borehole vertical electric transfer functions and TE-mode borehole vertical magnetic transfer functions (Z_{yx}, Z_{xy}, A_{xx}^d, A_{yy}^d, Z_{zx}^0 and T_y^0; Lagrange multiplier $\lambda = 10^{2.0}$; RMS = 1.00), **d** TM- and TE-mode surface impedances, TM- and TE-mode skin-effect transfer functions, TM-mode borehole vertical electric transfer functions and TE-mode borehole vertical magnetic transfer functions (Z_{yx}, Z_{xy}, A_{xx}^d, A_{yy}^d, Z_{zx}^0 and T_y^0; Lagrange multiplier $\lambda = 10^{2.0}$; RMS = 1.00) including data only from the right borehole. Black outlines and labels indicate structures of the true model in Fig. 9

The apparent resistivities and phases of the TM- and TE-mode impedances in Fig. 10a, b indicate a general decrease in resistivity with depth. The BBMT apparent resistivities at frequencies below 1 Hz contain a stronger signature of the conductive unit LP than the AMT apparent resistivities. However, the phases are affected by unit LP already at AMT frequencies.

In the first borehole at 4400 m along the profile, the skin-effect transfer functions A_{xx}^d and A_{yy}^d (Fig. 10c, d) indicate that the signal strengths of the TM and TE modes, respectively, have decayed to $< 10\%$ of their surface values at 500 m depth and frequencies $> 1\,\text{kHz}$, 750 m depth and frequencies $> 500\,\text{Hz}$, 1000 m depth and frequencies $> 200\,\text{Hz}$, and 1250 m depth and frequencies $> 100\,\text{Hz}$. The high level of similarity between A_{xx}^d and A_{yy}^d is related to the fact that the borehole is located in a model region which is close to 1D. As expected, the maximum absolute values of 0.06 V/A and 0.15 for the vertical electric and magnetic transfer functions Z_{zx}^0 and T_y^0 (Fig. 10e, f) are much smaller than those of the first example. Z_{zx} and T_y (not shown) are generally small in amplitude (mostly below 0.05 V/A and 0.1, respectively) but attain strongly localised maximum absolute values of 0.6 V/A and 0.4, respectively, at the upper boundary of unit SH and at the highest frequencies ($> 1\,\text{kHz}$). However, these peaks may be dominated by noise in actual field measurements owing to the low amplitudes of the electric and magnetic fields suggested by the skin-effect transfer functions at this position in the borehole and these frequencies.

In the second borehole at 5400 m along the profile (simulations not shown), the skin-effect transfer functions A_{xx}^d and A_{yy}^d are comparable to those of the first borehole but have a marginally lower decay rates with depth in the lower part of the borehole. Both Z_{zx} and Z_{zx}^0 are essentially zero (not shown), which is related to the absence of contrasts in electrical resistivity along the borehole. Only Z_{zx} has a low-amplitude anomaly of 0.25 V/A at depth $> 1300\,\text{m}$ and higher frequencies ($> 300\,\text{Hz}$). However, this peak may be dominated by noise in actual field measurements owing to the low amplitudes of the electric and magnetic fields suggested by the skin-effect transfer functions at these frequencies. In contrast, T_y and T_y^0 with absolute values as high as 0.4 at a depth of 1500 m may have more influence on the inversion models. The maxima occur at the bottom of the borehole, because the deepest borehole receiver has the closest proximity to the lateral structural boundaries between the resistive unit UDL and the conductive units PL and CZ.

4.2 2D Inversions

In Fig. 11, we present the models inverted from combinations of surface and borehole AMT and BBMT data. Prior to inversion, the synthetic responses presented in Fig. 10 were
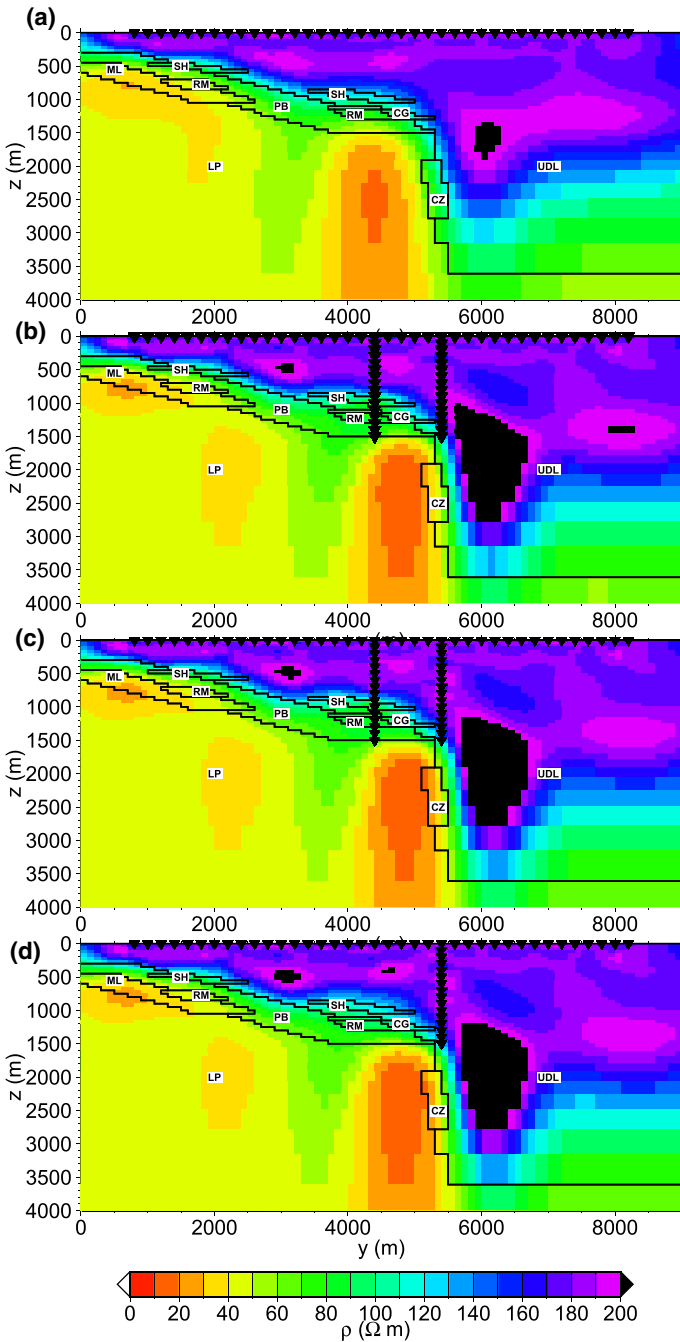
contaminated with the same levels of Gaussian noise as the data of the first example. In the inversions, we set the standard deviations of the data to correspond to the error levels employed for noise contamination. For this model, with a predominant decrease in

resistivity with depth and in line with our discussion until now, we demonstrate that addition of borehole measurements to surface measurements improves the inversion model only locally around the boreholes (zoom-in views of true model and inversion models in Fig. 12). A gross overall improvement in the resistivity model as that underneath the highly conductive shallow mineralisation in the first example cannot be observed.

4.2.1 Inversion of Surface AMT and BBMT Data

Starting from a homogeneous half space of $1000\,\Omega$m resistivity, it took the inversion algorithm 25 iterations to reach the model computed from our synthetic surface AMT and BBMT data (Z_{yx} and Z_{xy}) and presented in Fig. 11a. This model has an RMS misfit of 1.02. Most of the main features in the true model were reconstructed in this inversion model. The gross structures of units UDL, PB, RM, ML, CG and LP are in good or fair agreement with the true model in Fig. 9. However, the syngenetic halos (SH) are too resistive and the deep copper zone (CZ) is located about 800–900 m too far towards the beginning of the profile. Since the deep copper zone is located at the lateral contact between the conductive lower Palaeozoic unit and the more resistive upper dark limestones, and since the cross-sectional area of the lower Palaeozoic is much larger than that of the copper zone, the response by the copper zone might just be overprinted by that of the lower Palaeozoic. Additional inversions of surface impedance and VMTF data (not shown) seem to corroborate this assumption. Usually, VMTF data help to determine the horizontal positions of 2D or 3D resistivity anomalies. The initial model in the joint inversion of surface TM-mode impedance, TE-mode impedance and VMTF data was the best inversion model of the surface TM-mode and TE-mode impedances, i.e. the model presented in Fig. 11a. For the combined data set of surface TM-mode impedances, TE-mode impedances and VMTFs, this initial model has an RMS error of 1.02, i.e. almost the same total misfit as for the joint inversion of the surface TM-mode and TE-mode impedances. The best inversion model was computed in the third iteration and has an RMS of 0.99. Further iterations reduced the RMS to 0.98 but lead to rather rough models. Already the initial model explains the VMTF data very well and, consequently, there was not a lot of change in the model. In particular, the conceptual copper zone has an offset to the left from its true position almost identical to that in Fig. 11a.

4.2.2 Inversion of Surface and Borehole AMT and BBMT Data

After adding the skin-effect transfer functions A_{xx}^d and A_{yy}^d, we restarted the inversion from the model in Fig. 11a yielding an initial RMS misfit of 1.02. Only 3 iterations lead to the inversion model in Fig. 11b with an RMS misfit of 1.00. While the drop in total RMS misfit from 1.02 to 1.00 seems negligible, there is a slight improvement in the fit to A_{yy}^d which had its RMS misfit reduced from 1.06 to 1.02. The other skin-effect transfer function A_{xx}^d had an RMS misfit of 0.99 already for the initial model and was not explained better by the models computed during the inversion. As to be expected based on the small improvement in RMS misfit from the initial model to the model of the third iteration, the changes to the 2D model are very localised. In comparison with the model in Fig. 11a, the syngenetic halo penetrated by the borehole at 4400 m along the profile (cf. zoom-in views in Fig. 12) and the conceptual copper zone are in better agreement with the true model (Fig. 9).
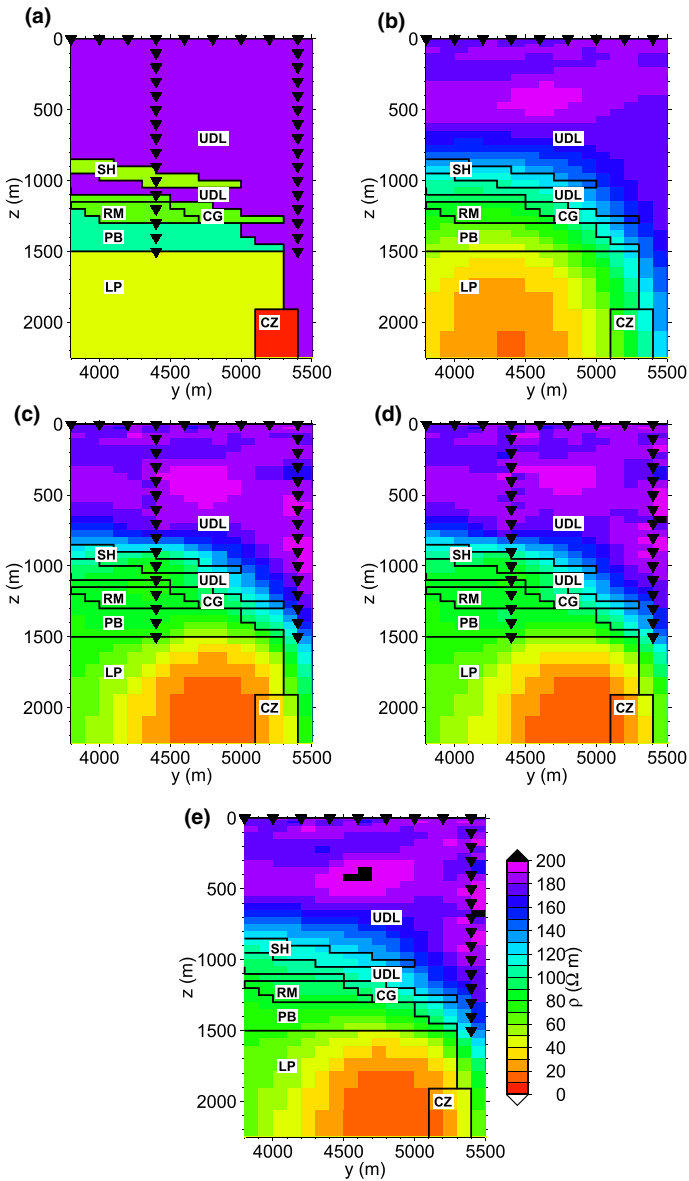
Fig. 12 Zoom-in views of **a** true model in Fig. 9 and **b–e** inversion models in Fig. 11a–d to a region around the boreholes. In comparison with the model computed from surface impedances in **b**, the inversion models in panels **c** and **d** that include the borehole skin-effect transfer functions and the complete set of borehole measurements, respectively, from both boreholes show a better resolved syngenetic halo (SH) and conceptual copper zone (CZ). The model in panel **e** computed from surface impedances and all data from the borehole at 5400 m along the profile shows better resolution only for the conceptual copper zone. Thus, data from the left borehole resolve the syngenetic halo, while data from the right borehole deliver constraints for the conceptual copper zone. Black outlines and labels indicate structures of the true model in Fig. 9

Finally, we added the vertical electric and magnetic transfer functions Z_{zx}^0 and T_y^0 to the data set to be inverted. Using the model in Fig. 11b as the initial model, the RMS misfit changed from 1.000 to 0.998 in the first iteration, after which the inversion process was terminated. The final model in Fig. 11c does not show any noticeable improvement over the model in Fig. 11b. Given the extremely small Z_{zx}^0 and T_y^0 responses for the true model (see above), it was to be expected that adding these transfer functions would neither add further information nor contribute to a more comprehensive image of the subsurface. We have also tested the inclusion of Z_{zx} and T_y instead of Z_{zx}^0 and T_y^0. While the former transfer functions have higher amplitudes than the latter, the improvement to the inversion model (not shown) in the form of changes to two cells at the top of unit SH penetrated by the borehole at 4400 m along the profile was still negligible.

For this second example, an inversion model (not shown) comparable to that in Fig. 11c could be obtained by directly inverting the combined AMT and BBMT surface and borehole data starting from the same initial model that was used to compute the model in Fig. 11a (a homogeneous half space of 1000 Ωm resistivity). Hence, for this case, with resistivity predominantly decreasing with depth and moderate resistivity contrasts, the three-step inversion scheme developed for the first example was not a prerequisite for a successful inversion process, and it was solely used to evaluate the benefits of including borehole measurements. Nevertheless, the improvements to the resistivity of the syngenetic halo (SH) penetrated by the first borehole and to the location of the copper zone (CZ) are significant.

A final inversion example in Fig. 11d for our second synthetic model illustrates the benefits that can be obtained when only the surface impedances and the A_{xx}^d, A_{yy}^d, Z_{zx}^0 and T_y^0 data of the second borehole at 5400 m along the profile are jointly inverted. As is to be expected from our evaluation of the forward responses of the synthetic model (Fig. 10), a combination of the surface impedances and the data from the borehole at 5400 m along the profile constrain the conceptual copper zone as well as the surface impedances and the data from both boreholes (model in Fig. 11c). However, as compared to the model computed from surface impedances only (Fig. 11a), there are no improvements in the model in Fig. 11d for the syngenetic halo and the red mineralisation intersected by the borehole at 4400 m along the profile.

5 Discussion and Conclusions

We have presented the first comprehensive 2D inversion studies of synthetic AMT and BBMT measurements on the surface and in boreholes based on two conceptual models of ore deposits. The considered data types include

- standard impedances of the TM and TE modes on the surface,
- standard vertical magnetic transfer functions of the TE mode on the surface,
- skin-effect transfer functions (vertical gradient magnetometry data) based on the horizontal magnetic fields of the TM and TE modes in boreholes and on the surface,
- the vertical magnetic transfer function of the TE mode based on the vertical magnetic field in boreholes and the horizontal magnetic field on the surface and
- the vertical electric transfer function of the TM mode based on the vertical electric field in boreholes and the horizontal magnetic field on the surface.

Our forward modelling and inversion results demonstrate that borehole measurements impose different levels of difficulty to handle in inversion. Whereas the skin-effect transfer functions are sensitive to the layered background medium and provide constraints for the resistivity structure laterally off and below the borehole, the vertical magnetic and electric transfer functions have little sensitivity to the resistivity distribution of the layered background medium and the vertical electric transfer function jumps across resistivity contrasts with the ratio of the resistivities. Thus, the vertical electric transfer function is predominantly sensitive to resistivity structure along the borehole and within a few hundred metres off the borehole. The low sensitivities of the vertical magnetic and electric transfer functions to the layered background medium, and the abrupt changes in the vertical electric transfer function across resistivity contrasts, require the initial model to be relatively close to the true model for the inversion to converge, if the resistivity contrasts are well pronounced (as in our first example). Consequently, we have developed a sequential inversion scheme involving three steps: (1) we compute a first inversion model using inversion of the impedances measured on the surface, (2) this first inversion model is used as an initial model in the inversion of surface impedances and skin-effect transfer functions and (3) the inversion model from the second step is used as an initial model in the inversion of surface impedances, skin-effect transfer functions and vertical magnetic and electric transfer functions. We have demonstrated that this sequential scheme leads to stable and meaningful inversion models. In cases with strong resistivity contrasts, there will be difficulty in converging to an inversion model that explains vertical electric transfer functions, if these are the only available borehole measurements.

Our inversion models exhibit significant improvement through addition of borehole measurements to the surface measurements. In particular, the addition of skin-effect transfer functions leads to improvement both in the vicinity of boreholes and at lateral distances of $\sim$ 300–1000 m off and at depth below boreholes. Addition of vertical magnetic and electric transfer functions can result in further improvement, but the vertical electric transfer function improves model constraints only in the vicinity of the borehole. The improvements are most obvious in our first example that is characterised by large resistivity contrasts and dipping conductive mineralisations embedded in resistive bedrock. In the inversion models, addition of borehole measurements has largely removed a conductive artefact at depth beneath the shallow conductor intersected by a borehole and demonstrated that the shallow and deep mineralisations are disparate units with the deep mineralisation being located in the along-dip extension of the shallow mineralisation. In the second example, the true model becomes generally more conductive with depth and the resistivity contrasts are small. Thus, we expected from the outset that the resistivity structure would already be well determined from MT measurements on the surface. Nevertheless, the MT measurements from the borehole at 4400 m along the profile that intersected a syngenetic halo led to quite accurate delineation of the top boundary of the syngenetic halo and MT measurements from the borehole at 5400 m along the profile that had its bottom 400 m above a conceptual copper zone captured the lateral position of the copper zone better than MT measurements on the surface. In our best inversion model that was derived from surface and borehole measurements, the right edge of the conceptual copper zone coincides with its left edge in the true model. Thus, there would be significantly greater chances in drilling the copper zone based on the model that includes borehole measurements than on the model that was computed using surface measurements only.

For our first example, we have quantified the model improvements by stating resolving kernels and errors of four cells in the different 2D inversion models. These model

resolution and error estimates were computed using linearisation of the forward operator. Since the smoothness-constrained most-squares inversion seems to work unreliably for data sets containing both surface and borehole measurements, the model error estimates from linearisation could not be compared to nonlinear estimates. Future attempts to compute nonlinear model error estimates may use a most-squares inversion based on singular value decomposition (Kalscheuer and Pedersen 2007), or an iterative procedure where the resistivity of the cell under investigation is fixed at a value smaller or larger than that of the preferred inversion model, and the remaining model parameters are allowed to vary freely in a subsequent inversion. This latter procedure would have to be repeated iteratively with further adjustment of the considered model parameter until the misfit functional assumes the value that corresponds to minus or plus one standard deviation of the model parameter (cf. Kalscheuer and Pedersen 2007; Kalscheuer et al. 2010).

Our forward simulations have clearly demonstrated that borehole magnetic field sensors to be used in the AMT frequency range need to be at least equally sensitive or up to five times more sensitive than state-of-the-art surface sensors, which are induction coils. Due to the limited space in slim boreholes, induction magnetometers cannot be used to record high-quality data of the off-axial components. However, in the AMT frequency range, sensitivities of modern SQUID magnetometers for surface measurements are comparable to the best induction magnetometers. Given that SQUID sensors only have a side length of 2 cm, they could be used in slim boreholes, if a sufficiently miniaturised cryogenic cooling system was available. In a continuation of this project, it is intended to develop a 3C HTS SQUID magnetometer for borehole measurements that has sensitivity comparable to surface 3C HTS SQUIDs ($10\,\mathrm{fT}/\sqrt{\mathrm{Hz}}$ at 10–10,000 Hz). A quantitative comparison of a newly developed SQUID sensor and state-of-the-art induction coil sensors for surface measurements is planned to be performed using AMT acquisition systems developed at the Department of Earth Sciences, Uppsala University. For BBMT signals at frequencies below 1 Hz, a borehole fluxgate sensor should be developed or existing commercial sensors that were originally developed for time-domain or frequency-domain BHEM systems should be modified to measure BBMT signals.

Through measurements at depth using improved sensor technology, it can become possible to achieve a better delineation of ore bodies than with surface AMT and BBMT measurements alone. It is anticipated that borehole AMT and BBMT measurements may improve resolution for ore bodies traversed by the borehole sensor and of the upper edges of ore bodies at greater depth below the borehole. Hence, inclusion of borehole AMT and BBMT measurements with highly sensitive 3C SQUID and fluxgate magnetometers and vertical (or axial) electric field sensors may contribute to more detailed descriptions of potential ore deposits than possible with present-day techniques. It is reasonable to assume that the inclusion of variable magnetic susceptibility in the 2D inversion code is needed to facilitate meaningful 2D inversion of AMT and BBMT data from ore deposits with strongly magnetic rocks. Furthermore, consideration of anisotropic resistivity may be necessary to fully describe mineralised zones. Nevertheless, the borehole AMT and BBMT techniques suggested here are not limited to application in ore exploration. Further fields that will benefit from the proposed methods are, for instance, geothermal exploration, energy storage, hydrological and tectonic studies.

Further improvements in models of mineral deposits can be obtained by including resistivity borehole logs as local prior information (e.g., Yan et al. 2017a), by transferring structural boundaries observed in reflection seismic images or seismic velocity models to 2D or 3D inversion models of MT data (e.g., Le et al. 2016b; Yan et al. 2017b; Moorkamp

2017) or by performing joint inversions of MT, seismic and potential field data using petrophysical or structural coupling (e.g., Moorkamp et al. 2011; Gallardo and Meju 2011; Haber and Gazit 2013; Takam Takougang et al. 2015; Moorkamp 2017). Strictly speaking, well logs only represent the resistivity structure up to a few metres off the borehole and may be affected by borehole fluids and the invaded zone around the borehole. How far the logging resistivities are actually propagated as information into a 2D or 3D resistivity model depends on the employed smoothness constraints and to what extent data from adjacent MT stations are compatible with this prior information. In total, resistivity logs as prior constraints are not at all as influential on the inversion model, in terms of the volume that is constrained as are MT field sensors at depth. Inclusion of seismic constraints, for instance, by deriving smoothness constraints for the inversion of MT data from seismic attributes, has proved to be effective and to lead to geologically more meaningful inversion models. To accurately outline mineral deposits, we advocate a comprehensive approach to model construction including surface and borehole MT and CSEM measurements, borehole logs, seismic measurements and potential field measurements.

Appendix: Verification of Finite-Difference Method

The correctness of the finite-difference forward solver was verified by comparison with semi-analytic and finite-difference solutions for a control model consisting of three conductive segments overlying a perfectly conductive half space presented by Weaver et al. (1985, 1986) for the TM- and TE-modes, respectively. Weaver et al. (1985, 1986) tabulate forward responses simulated at the surface and at 15 km depth. To obtain correct finite-difference results for the lower boundary of the computational domain that coincides with the top of a perfectly conductive half space as in the control model, Neumann boundary conditions need to be used at the lower edge of the mesh in the TM-mode (Brewitt-Taylor and Weaver 1976; Weaver et al. 1985). Brewitt-Taylor and Weaver (1976) implemented Neumann boundary conditions using single sided approximations, reducing the order of the finite-difference approximation to first order. To achieve better computational accuracy, the approach presented here follows LeVeque (2007) and uses a centred second-order approximation of the first derivative employing ghost nodes one fictitious cell height below the lower boundary of the computational domain. Combining this centred approximation to the Neumann boundary condition and the Helmholtz equation of the TM-mode (e.g., eq. 14 in Kalscheuer et al. 2008) eliminates the horizontal magnetic fields of the ghost

nodes from the system of linear equations. Using this approach, the system matrix remains tri-diagonal and banded, but looses its complex symmetry. For the finite-difference algorithm used here, this did not pose a serious limitation, because the originally complex symmetric matrix was factored using LU decomposition anyhow.

In the central part of the control model, we used the same finite-difference grid as employed by Weaver et al. (1985, 1986). However, to account for differences in TE-mode boundary conditions, we used a larger number of padding cells in the air and at the left and right edges of the mesh. The results of the finite-difference equations used by us have typical deviations of less than 1.5% from Weaver et al.'s (1985, 1986) semi-analytic solutions for the TM- and TE-modes. In general, the accuracy of our finite-difference solution is comparable to Weaver et al.'s (1985, 1986) finite-difference solutions. Note that closer proximity to the semi-analytic solutions can be obtained by employing a finer discretisation in the central part of the mesh.

References

Asten MW (1988) The down-hole magnetometric resistivity (DHMMR) method. Explor Geophys 19(1–2):12–16

Asten MW (1996) Drillhole EM—a strictly scientific hokey-pokey. Explor Geophys 27(2–3):41–49

Asten MW (2001) Borehole EM and MMR methods for weak conductors—a project review. In: ASEG 15th geophysical conference and exhibition, Brisbane, p ab002

Asten MW, Duncan AC (2012) The quantitative advantages of using B-field sensors in time-domain EM measurement for mineral exploration and unexploded ordnance search. Geophysics 77(4):WB137–WB148

Bahr K (1983) Joint interpretation of magnetotelluric and geomagnetic data and local telluric distortions. J Geomagn Geoelectr 35(11–12):555–566

Bahr K, Eisel M (1990) Vertikale tellurische Pulsationen in der KTB-Vorbohrung: laterale Leitfähigkeitskontraste und virtuelle zeitliche Variationen des Eigenpotentials. In: KTB Report, vol 90-6a, pp 179–189

Balch SJ, Crebs TJ, King A, Verbiski M (1998) Geophysics of the Voisey's Bay Ni–Cu–Co deposits. In: SEG Technical program expanded abstracts, vol 1998, pp 784–787

Basokur AT, Rasmussen TM, Kaya C, Altun Y, Aktas K (1997) Comparison of induced polarization and controlled-source audio-magnetotellurics methods for massive chalcopyrite exploration in a volcanic area. Geophysics 62(4):1087–1096

Bastani M, Malehmir A, Ismail N, Pedersen LB, Hedjazi F (2009) Delineating hydrothermal stockwork copper deposits using controlled-source and radio-magnetotelluric methods: a case study from northeast Iran. Geophysics 74(5):B167–B181

Becken M, Ritter O, Burkhardt H (2008) Mode separation of magnetotelluric responses in three-dimensional environments. Geophys J Int 172(1):67–86

Bedrosian PA (2007) MT+, integrating magnetotellurics to determine Earth structure, physical state, and processes. Surv Geophys 28(2):121–167

Berdichevsky MN, Dmitriev VI (2008) Models and methods of magnetotellurics. Springer, Berlin

Berdichevsky MN, Dmitriev VI, Pozdnjakova EE (1998) On two-dimensional interpretation of magnetotelluric soundings. Geophys J Int 133(3):585–606

Berktold A (1983) Electromagnetic studies in geothermal regions. Geophys Surv 6(1):173–200

Bick M, Panaitov G, Wolters N, Zhang Y, Bousack H, Braginski AI, Kalberkamp U, Burkhardt H, Matzander U (1999) A HTS rf SQUID vector magnetometer for geophysical exploration. IEEE Trans Appl Supercond 9(2):3780–3785

Bishop J, Carroll N, Asten M, Hatch M, Macinnes S (1997) Finding sphalerite at Broken Hill with drillhole magnetometric resistivity. Explor Geophys 28(1–2):6–10

Bishop JR, Lewis R, Stolz N (2000) Horses for (conductive) courses: DHEM and DHMMR. Explor Geophys 31(2):192–199

Box GEP, Muller ME (1958) A note on the generation of random normal deviates. Ann Math Stat 29(2):610–611

Boyd GW, Wiles CJ (1984) The Newmont drill-hole EMP system—examples from eastern Australia. Geophysics 49(7):949–956

Brasse H, Rath V (1997) Audiomagnetotelluric investigations of shallow sedimentary basins in northern Sudan. Geophys J Int 128(2):301–314

Brewitt-Taylor CR, Weaver JT (1976) On the finite difference solution of two-dimensional induction problems. Geophys J R astr Soc 47(2):375–396

Chave AD, Booker JR (1987) Electromagnetic induction studies. Rev Geophys 25(5):989–1003

Chave AD, Jones AG (eds) (2012) The Magnetotelluric method: theory and practice. Cambridge University Press, Cambridge

Chen J, Haber E, Oldenburg DW (2002) Three-dimensional numerical modelling and inversion of magnetometric resistivity data. Geophys J Int 149(3):679–697

Chouteau M, Zhang P, Dion DJ, Giroux B, Morin R, Krivochieva S (1997) Delineating mineralization and imaging the regional structure with magnetotellurics in the region of Chibougamau (Canada). Geophysics 62(3):730–748

Chwala A, Stolz R, Ramos J, Schultze V, Meyerd HG, Kretzschmar D (1999) An HTS dc SQUID system for geomagnetic prospection. Supercond Sci Technol 12(11):1036–1038

Clarke J (1983) Geophysical applications of SQUIDs. IEEE Trans Magn 19(3):288–294

Constable S (2013) Review paper: instrumentation for marine magnetotelluric and controlled source electromagnetic sounding. Geophys Prospect 61(s1):505–532

Crowe M, Heinson G, Dhu T (2013) Magnetotellurics and airborne electromagnetics—a combined method for assessing basin structure and exploring for unconformity-related uranium. In: ASEG extended abstracts 2013, 23rd geophysical conference, pp 1–5

Cull JP (1996a) Rotation and resolution of three-component DHEM data. Explor Geophys 27(2–3):155–159

Cull JP (1996b) Sensor response and resolution in downhole TEM data. Explor Geophys 27(2–3):167–169

Duncan A, Amann B, O'Keeffe K, Williams P, Tully T, Wellington A, Turner G (1998) Examples from a new EM and electrical methods receiver system. Explor Geophys 29(4):347–354

Dyck AV (1991) Drill-hole electromagnetic methods. In: Nabighian (1991), chap 3, pp 881–930

Edwards RN, Nabighian MN (1991) The magnetometric resistivity method. In: Nabighian (1991), chap 3, pp 47–104

Elders JA, Asten MW (2004) A comparison of receiver technologies in borehole MMR and EM surveys. Geophys Prospect 52(2):85–96

Farquharson CG, Craven JA (2009) Three-dimensional inversion of magnetotelluric data for mineral exploration: an example from the McArthur River uranium deposit, Saskatchewan, Canada. J Appl Geophys 68(4):450–458

Ferguson IJ (2012) Instrumentation and field procedures. In: Chave and Jones (2012), chap 9, pp 421–479

Forbush SE (1933) Apparent vertical Earth-current variations at the Huancayo Magnetic Observatory. Terr Magn Atmos Electr 38(1):1–11

Fullagar PK, Livelybrooks DW, Zhang P, Calvert AJ, Wu Y (2000) Radio tomography and borehole radar delineation of the McConnell nickel sulfide deposit, Sudbury, Ontario, Canada. Geophysics 65(6):1920–1930

Gallardo LA, Meju MA (2011) Structure-coupled multiphysics imaging in geophysical sciences. Rev Geophys 49:RG1003

Garcia X, Jones AG (2002) Atmospheric sources for audio-magnetotelluric (AMT) sounding. Geophysics 67(2):448–458

Garcia Juanatey M, Hübert J, Tryggvason A, Pedersen LB (2013a) Imaging the Kristineberg mining area with two perpendicular magnetotelluric profiles in the Skellefte Ore District, northern Sweden. Geophys Prospect 61(1):200–219

Garcia Juanatey M, Tryggvason A, Juhlin C, Bergström U, Hübert J, Pedersen LB (2013b) MT and reflection seismics in northwestern Skellefte Ore District, Sweden. Geophysics 78(2):B65–B76

Godber KE, Bishop JR (2007) DHMMR: coming of age. In: Milkereit B (ed) Proceedings of Exploration 07: fifth decennial international conference on mineral exploration, pp 1119–1123

Goldak D, Witherly K, Kosteniuk P (2010) Three-dimensional inversion of transient magnetotelluric data at Pasfield Lake, Saskatchewan. In: SEG Technical program expanded abstracts 2010, pp 859–863

Gordon RL (2007) An integrated 3D approach to deep search exploration. In: Milkereit B (ed) Proceedings of Exploration 07: fifth decennial international conference on mineral exploration, pp 551–560

Haber E, Gazit MH (2013) Model fusion and joint inversion. Surv Geophys 34(5):675–695

Hattula A, Rekola T (2000) Exploration geophysics at the Pyhasalmi mine and grade control work of the Outokumpu Group. Geophysics 65(6):1961–1969

Hautot S, Goldak D, Tarits P, Kosteniuk P (2011) Three-dimensional magnetotelluric inversion of large data sets: case study of Pasfield Lake (Saskatchewan) for mineral exploration. In: International workshop on gravity, electrical and magnetic methods and their applications, Beijing, China, October 10–13, 2011

Hayles JG, Dyck AV (1987) Borehole electrical surveys as an aid to structural mapping, Chalk River, Ontario—a feasibility study. In: Thomas MD, Dixon DF (eds) Geophysical and related geoscientific reseach at Chalk River, Ontario, vol Report AECL-9085. Atomic Energy of Canada Ltd., Chalk River, pp 309–328

Heinson GS, Direen NG, Gill RM (2006) Magnetotelluric evidence for a deep-crustal mineralizing system beneath the Olympic Dam iron oxide copper-gold deposit, southern Australia. Geology 34(7):573–576

Hermance JF, Slocum WM, Neumann GA (1984) The Long Valley/Mono Basin Volcanic Complex: a preliminary magnetotelluric and magnetic variation interpretation. J Geophys Res 89(B10):8325–8337

Howe BD, Townsend J, Doerner B, Patraskovic P (2014) Three-dimensional magnetotelluric inversion and petrophysical interpretation of the Turquoise Ridge gold deposit, Nevada, USA. In: SEG technical program expanded abstracts 2014, pp 1730–1735

Hu X, Peng R, Wu G, Wang W, Huo G, Ha B (2013) Mineral exploration using CSAMT data: Application to Longmen region metallogenic belt, Guangdong Province, China. Geophysics 78(3):B111–B119

Hübert J, Garcia Juanatey M, Malehmir A, Tryggvason A, Pedersen LB (2013) The upper crustal 3-D resistivity structure of the Kristineberg area, Skellefte district, northern Sweden revealed by magnetotelluric data. Geophys J Int 192(2):500–513

Hübert J, Lee BM, Liu L, Unsworth MJ, Richards JP, Abbassi B, Cheng LZ, Oldenburg DW, Legault JM, Rebagliati M (2016) Three-dimensional imaging of a Ag–Au-rich epithermal system in British Columbia, Canada, using airborne z-axis tipper electromagnetic and ground-based magnetotelluric data. Geophysics 81(1):B1–B12

Hughes NA, Ravenhurst WR (1996) Three component DHEM surveying at Balcooma. Explor Geophys 27(2–3):77–89

Jegen M, Edwards RN (1998) The electrical properties of a 2D conductive zone under the Juan de Fuca Ridge. Geophys Res Lett 25(19):3647–3650

Jones AG (1983) A passive natural-source twin-purpose borehole technique: vertical gradient magnetometry (VGM). J Geomagn Geoelectr 35(11–12):473–490

Jones AG (1999) Imaging the continental upper mantle using electromagnetic methods. Lithos 48(1–4):57–80

Jones AG (2012) Distortion of magnetotelluric data: its identification and removal. In: Chave and Jones (2012), chap 6, pp 219–302

Jones AG (2017) Magnetotellurics: status quo and quo vadimus. In: Tschirhart V, Thomas MD (eds) Proceedings of Exploration 17: sixth decennial international conference on mineral exploration, pp 139–158

Jones AG, Garcia X (2003) Okak Bay AMT data-set case study: lessons in dimensionality and scale. Geophysics 68(1):70–91

Jones AG, Katsube TJ, Schwann P (1997) The longest conductivity anomaly in the world explained: sulphides in fold hinges causing very high electrical anisotropy. J Geomagn Geoelectr 49(11–12):1619–1629

Jones FW, Geldart LP (1967a) Vertical telluric currents. Earth Planet Sci Lett 2(1):69–74

Jones FW, Geldart LP (1967b) Vertical telluric currents at separated locations. Earth Planet Sci Lett 2(3):174–176

Joseph EJ, Toh H, Fujimoto H, Iyengar R, Singh B, Utada H, Segawa J (2000) Seafloor electromagnetic induction studies in the Bay of Bengal. Mar Geophys Res 21(1):1–21

Kalberkamp U, Matzander U, Husemann KD, Panaitow G, Zimmermann E, Zhang Y (1997) HTS rf-SQUID applications to geophysical exploration methods. Appl Supercond 5(7–12):205–211

Kalscheuer T, Pedersen LB (2007) A non-linear truncated SVD variance and resolution analysis of two-dimensional magnetotelluric models. Geophys J Int 169(2):435–447

Kalscheuer T, Pedersen LB, Siripunvaraporn W (2008) Radiomagnetotelluric two-dimensional forward and inverse modelling accounting for displacement currents. Geophys J Int 175(2):486–514

Kalscheuer T, Garcia Juanatey M, Meqbel N, Pedersen LB (2010) Non-linear model error and resolution properties from two-dimensional single and joint inversions of direct current resistivity and radio-magnetotelluric data. Geophys J Int 182(3):1174–1188

Kalscheuer T, Blake S, Podgorski JE, Wagner F, Green AG, Muller M, Jones AG, Maurer H, Ntibinyane O, Tshoso G (2015) Joint inversions of three types of electromagnetic data explicitly constrained by seismic observations: results from the central Okavango Delta, Botswana. Geophys J Int 202(3):1429–1452

Kellett R, Bishop J, Reed EV (1993) The effects of source polarization in CSAMT data over two massive sulfide deposits in Australia. Geophysics 58(12):1764–1772

King A (2007) Review of geophysical technology for Ni-Cu-PGE deposits. In: Milkereit B (ed) Proceedings of Exploration 07: fifth decennial international conference on mineral exploration, pp 647–665

Lakanen E (1986) Scalar audiomagnetotellurics applied to base-metal exploration in Finland. Geophysics 51(8):1628–1646

Law LK, Greenhouse JP (1981) Geomagnetic variation sounding of the asthenosphere beneath the Juan de Fuca Ridge. J Geophys Res 86(B2):967–978

Le CVA, Harris BD, Pethick AM (2016a) Magnetotelluric inversion, carbonaceous phyllites and an ore zone: Kevitsa, Finland. In: ASEG extended abstracts 2016: 25th international geophysical conference and exhibition, pp 525–529

Le CVA, Harris BD, Pethick AM, Takam Takougang EM, Howe B (2016b) Semiautomatic and automatic cooperative inversion of seismic and magnetotelluric data. Surv Geophys 37(5):845–896

Le Roux C, Macnae J (2007) SQUID sensors for EM systems. In: Milkereit B (ed) Exploration in the new millennium: proceedings of the fifth decennial international conference on mineral exploration, pp 417–423

Lee JB, Dart DL, Turner RJ, Downey MA, Maddever A, Panjkovic G, Foley CP, Leslie KE, Binks R, Lewis C, Murray W (2002) Airborne TEM surveying with a SQUID magnetometer sensor. Geophysics 67(2):468–477

Leppin M, Goldak D (2005) Mapping deep sandstone alteration and basement conductors utilizing audio magnetotellurics: exploration for uranium in the Virgin River area, Athabasca Basin, Saskatchewan, Canada. In: SEG Technical Program Expanded Abstracts 2005, SEG

LeVeque RJ (2007) Finite difference methods for ordinary and partial differential equations: steady-state and time-dependent problems. Society for industrial and applied mathematics, Philadelphia, PA

Liu H, Liu J, Yu C, Ye J, Zeng Q (2006) Integrated geological and geophysical exploration for concealed ores beneath cover in the Chaihulanzi goldfield, northern China. Geophys Prospect 54(5):605–621

Livelybrooks D, Mareschal M, Blais E, Smith JT (1996) Magnetotelluric delineation of the Trillabelle massive sulfide body in Sudbury, Ontario. Geophysics 61(4):971–986

McGillivray PR, Oldenburg DW (1990) Methods for calculating Fréchet derivatives and sensitivities for the non-linear inversion problem: a comparative study. Geophys Prospect 38(5):499–524

Meju MA (1994) Biased estimation: a simple framework for inversion and uncertainty analysis with prior information. Geophys J Int 119(2):521–528

Meju MA (2002) Geoelectromagnetic exploration for natural resources: models, case studies and challenges. Surv Geophys 23(2–3):133–206

Meju MA, Hutton VRS (1992) Iterative most-squares inversion: application to magnetotelluric data. Geophys J Int 108(3):758–766

Menke W (2015) Review of the generalized least squares method. Surv Geophys 36(1):1–25

Moorkamp M (2017) Integrating electromagnetic data with other geophysical observations for enhanced imaging of the earth: a tutorial and review. Surv Geophys 38(5):935–962

Moorkamp M, Heincke B, Jegen M, Roberts AW, Hobbs RW (2011) A framework for 3-D joint inversion of MT, gravity and seismic refraction data. Geophys J Int 184(1):477–493

Mwenifumbo CJ, Elliott BE, Cinq-Mars A (1997) Field evaluation of a four-component downhole VLF-EM logging system. In: Gubins AG (ed) Proceedings of Exploration 97: fourth decennial international conference on mineral exploration, pp 541–544

Nabighian MN (ed) (1991) Electromagnetic methods in applied geophysics, vol 2, Applications, Parts A and B. SEG, Tulsa

Nabighian MN, Oppliger GL, Edwards RN, Lo BBH, Cheesman SJ (1984) Cross-hole magnetometric resistivity (MMR). Geophysics 49(8):1313–1326

Panaitov G, Bick M, Zhan Y, Krause HJ (2002) Peculiarities of SQUID magnetometer application in TEM. Geophysics 67(3):739–745

Pantze R, Malmqvist L, Kristensson G (1986) Directional EM measurements in boreholes. In: Killeen PG (ed.) Borehole geophysics for mining and geotechnical applications, vol paper 85–27, Geological Suvey of Canada, pp 79–88

Pedersen LB, Engels M (2005) Routine 2D inversion of magnetotelluric data using the determinant of the impedance tensor. Geophysics 70(2):G33–G41

Press WH, Flannery BP, Teukolsky SA, Vetterling WT (1991) Numerical recipes in Pascal: the art of scientific computing, 1st edn. Cambridge University Press, Cambridge

Queralt P, Jones AG, Ledo J (2007) Electromagnetic imaging of a complex ore body: 3D forward modeling, sensitivity tests, and down-mine measurements. Geophysics 72(2):F85–F95

Rao CK, Jones AG, Moorkamp M, Weckmann U (2014) Implications for the lithospheric geometry of the Iapetus suture beneath Ireland based on electrical resistivity models from deep-probing magnetotellurics. Geophys J Int 198(2):737–759

Rodi W, Mackie RL (2001) Nonlinear conjugate gradients algorithm for 2-D magnetotelluric inversion. Geophysics 66(1):174–187

Roy J (1984) Electrical methods in mineral well logging. Ph.D. thesis, McGill University

Sasaki Y, Yoneda Y, Matsuo K (1992) Resistivity imaging of controlled-source audiofrequency magnetotelluric data. Geophysics 57(7):952–955

Schmucker U, Spitzer K, Steveling E (2009) An electromagnetic sounding experiment in Germany using the vertical gradient of geomagnetic variations observed in a deep borehole. Geophys J Int 178(3):1273–1288

Smith RS (2014) Electromagnetic induction methods in mining geophysics from 2008 to 2012. Surv Geophys 35(1):123–156

Spicer B (2016) Geophysical signature of the Victoria property, vectoring toward deep mineralization in the Sudbury Basin. Interpretation 4(3):T281–T290

Spies BR (1996) Electrical and electromagnetic borehole measurements: a review. Surv Geophys 17(4):517–556

Spitzer K (1993) Observations of geomagnetic pulsations and variations with a new borehole magnetometer down to depths of 3000 m. Geophys J Int 115(3):839–848

Sternberg BK (2010) The variability of naturally occurring magnetic field levels: 10 Hz to 8 kHz. Geophysics 75(6):F187–F197

Steveling E, Spitzer K, Leven M (1991) Vertical gradient of horizontal geomagnetic variations—first results with the Göttingen borehole magnetometer in the KTB-Oberpfalz VB. Sci Drill 2:180–187

Stevens KM, McNeice G (1998) On the detection of Ni–Cu ore hosting structures in the Sudbury Igneous Complex using the magnetotelluric method. In: SEG technical program expanded abstracts 1998, pp 751–755

Strangway DW, Swift CM, Holmer RC (1973) The application of audio frequency magnetotellurics (AMT) to mineral exploration. Geophysics 38(6):1159–1175

Takam Takougang EM, Harris B, Kepic A, Le CVA (2015) Cooperative joint inversion of 3D seismic and magnetotelluric data: with application in a mineral province. Geophysics 80(4):R175–R187

Tuncer V, Unsworth MJ, Siripunvaraporn W, Craven JA (2006) Exploration for unconformity-type uranium deposits with audiomagnetotelluric data: a case study from the McArthur River mine, Saskatchewan, Canada. Geophysics 71(6):B201–B209

Vallee MA, Smith RS, Keating P (2011) Metalliferous mining geophysics—state of the art after a decade in the new millennium. Geophysics 76(4):W31–W50

Varentsov IM, Kulikov VA, Yakovlev AG, Yakovlev DV (2013) Possibilities of magnetotelluric methods in geophysical exploration for ore minerals. Izvestiya Phys Solid Earth 49(3):309–328

Vozoff K (1991) The magnetotelluric method. In: Nabighian (1991), chap 8, pp 641–711

Ward SH, Hohmann GW (1987) Electromagnetic theory for geophysical applications. In: Nabighian MN (ed) Electromagnetic methods in applied geophysics, vol 1, Theory, SEG, Tulsa, chap 4, pp 131–311

Watts MD, Balch SJ (2000) AEM-constrained 2D inversion of AMT data over the Voisey's Bay massive sulfide body, Labrador. In: SEG technical program expanded abstracts 2000, pp 1119–1121

Weaver JT, Le Quang BV, Fischer G (1985) A comparison of analytical and numerical results for a two-dimensional control model in electromagnetic induction—I. B-polarization calculations. Geophys J R Astr Soc 82(2):263–277

Weaver JT, Le Quang BV, Fischer G (1986) A comparison of analytical and numerical results for a two-dimensional control model in electromagnetic induction—II. E-polarization calculations. Geophys J R Astr Soc 87(3):917–948

Weckmann U, Ritter O, Jung A, Branch T, de Wit M (2007) Magnetotelluric measurements across the Beattie magnetic anomaly and the Southern Cape Conductive Belt, South Africa. J Geophys Res 112(5):B05,416

West RC, Ward SH (1988) The borehole controlled-source audiomagnetotelluric response of a three-dimensional fracture zone. Geophysics 53(2):215–230

Xiao Q, Cai X, Liang G, Xu X, Zhang B (2011) Application of 2D magnetotelluric methods in a geological complex area, Xinjiang, China. J Appl Geophys 75(1):19–30

Yan P, Garcia Juanatey M, Kalscheuer T, Juhlin C, Hedin P, Savvaidis A, Lorenz H, Kück J (2017a) A magnetotelluric investigation of the Scandinavian Caledonides in western Jämtland, Sweden, using the COSC borehole logs as prior information. Geophys J Int 208(3):1465–1489

Yan P, Kalscheuer T, Hedin P, Garcia Juanatey M (2017b) Two-dimensional magnetotelluric inversion using reflection seismic data as constraints and application in the COSC project. Geophys Res Lett 44(8):3554–3563

Zhang P, King A, Watts D (1998) Using magnetotellurics for mineral exploration. In: SEG technical program expanded abstracts 1998, pp 776–779

Zonge KL, Hughes LJ (1991) Controlled source audio-frequency magnetotellurics. In: Nabighian (1991), chap 9, pp 713–809